Understanding Electrolyte Filling of Lithium-Ion Battery Electrodes on the Pore Scale Using the Lattice Boltzmann Method

Martin P. Lautenschlaeger[a,b,*], Benedikt Prifling[c], Benjamin Kellers[a,b], Julius Weinmiller[a,b], Timo Danner[a,b], Volker Schmidt[c], Arnulf Latz[a,b,d]

[a] *German Aerospace Center (DLR), Institute of Engineering Thermodynamics, 70569 Stuttgart, Germany*
[b] *Helmholtz Institute Ulm for Electrochemical Energy Storage (HIU), 89081 Ulm, Germany*
[c] *Ulm University (UUlm), Institute of Stochastics, 89081 Ulm, Germany*
[d] *Ulm University (UUlm), Institute of Electrochemistry, 89081 Ulm, Germany*

Abstract

Electrolyte filling is a time-critical step during battery manufacturing that also affects the battery performance. The underlying physical phenomena during the filling process mainly occur on the pore scale and are hard to study experimentally. Therefore, they are still not well understood. In the present work, a computational approach, i.e. the lattice Boltzmann method, is used to study the filling process and the corresponding pore-scale phenomena, where the electrolyte flow in 3D lithium-ion battery cathodes is simulated with high spatial resolution. The electrolyte flow through the nanoporous binder phase is simulated using a homogenization approach. Besides the process time, the influence of structural and physico-chemical properties is investigated. Those are the particle size of the active material, the distribution of binder, as well as the volume fraction and the wetting behavior of both the active material and the binder. Optimized filling conditions are discussed by means of capillary pressure-saturation relationships during filling. It is shown how the aforementioned influencing factors affect the electrolyte saturation with a maximum of entrapped gas phase up to 37 %. Moreover, the amount of the entrapped residual gas phase and the corresponding size distribution of the gas agglomerates are analyzed in detail. Both factors are shown to have a strong impact on mechanisms that can adversely affect the battery performance. The results obtained here indicate how the

---

[*] Corresponding author:
Email address: `Martin.Lautenschlaeger@dlr.de` (Martin P. Lautenschlaeger)

filling process, the final degree of electrolyte saturation, and potentially also the battery performance can be optimized by adapting process parameters as well as the electrode and electrolyte design.

Keywords: lattice Boltzmann method, Li-ion battery, two-phase flow, gas entrapment, microstructure

---

1. Introduction

Lithium-ion batteries are the major power source for battery electric vehicles. Its cell production is predicted to increase exponentially in the upcoming years. Therefore, the optimization of the battery production is key to reduce costs and the environmental impact of next-generation battery cells. Improving the battery manufacturing process requires the optimization of each process step. One of the process steps that has recently gained attention in this context, is the filling of cells with liquid electrolyte, where the electrolyte is first dosed into the cell and subsequently stored to achieve a uniform electrolyte distribution. Sometimes dosing and storing are even repeated to decrease the amount of residual gas being entrapped in the pore space [1, 2]. Thus, from an economical standpoint, the filling process is time-consuming and cost-intensive. It can take up to several days [1, 3, 4]. Additionally, the filling process was shown to also affect the battery performance and lifetime [3–6]. It is known that poorly wetted pores in the electrodes cause the development of an inhomogeneous solid electrolyte interphase (SEI) [7]. Moreover, they can lead to electrolyte decomposition during cycling [8], dendrite formation [1, 5, 9], as well as non-uniform current densities [4, 10]. An incomplete wetting can also have a large effect on the battery performance by increasing internal ionic resistances remarkably, which has recently been investigated for separators [11].

There are different strategies to prevent the aforementioned limitations and to increase the wettability as well as the final degree of electrode saturation. On the one hand, the filling process can be sped up by an evacuation of the cells and application of pressure gradients along the filling direction [1–3, 5, 12]. Thereby, the filling duration can be reduced by up to 50 % [4]. On the other hand, tuning the physico-chemical properties of electrolyte and electrodes can also improve the filling process [11]. Two main approaches are considered in the literature. Either electrolyte properties, i.e. surface tension and viscosity, are adjusted by adding additives to the electrolyte [12, 13] or the surface wettability of electrodes is improved using coatings or surfactants [6]. Moreover, also the structural properties of electrodes and separator are known to have a significant influence on the filling process [1, 2, 6, 9, 11, 14]. The compaction of the electrode by calendering, e.g., increases the filling duration and the amount of residual gas in the pores [1, 2, 6, 14].

Recently, different experimental studies have tried to shed light on the time behavior of the filling process by applying in-situ methods. Amongst those were electrochemical impedance spectroscopy [15], neutron radiography [2–4], X-ray measurements [9], focused ion beam combined with scanning electron microscopy [14], thermography [6], and wetting balance tests [6]. However, most of those methods are complex and time-consuming. Moreover, they all suffer from low spatial or temporal resolution, imprecise localization of the wetting front, or cannot resolve the interdependency of the different influencing factors. Thus, a comprehensive understanding especially of pore-scale phenomena during the filling process is missing [14]. There is still no common agreement on how to optimize this process step, especially when taking into account the multitude of electrochemical systems and cell types available on the market [5].

A method that is capable of giving a detailed insight into the wetting phenomena and the interdependency of the different influencing factors are direct numerical simulations on the pore scale in general, and the lattice Boltzmann method (LBM) in particular. In the past years, LBM has proven to be a reliable tool for the simulation of transport processes and fluid flow [16, 17]. In contrast to conventional fluid dynamics, it has the big advantage of giving access to multi-scale and multi-physics issues even within complex geometries, e.g., in porous media [18, 19].

The multi-component Shan-Chen pseudopotential method (MCSC) has regularly been utilized to simulate multi-phase flows with LBM [18–20]. Similar to molecular dynamics simulations, where molecular interactions are modeled to study, e.g., wetting phenomena [21–23] or transport processes [24, 25], it uses fluid-fluid and solid-fluid interaction forces to model interfacial tension and adhesion forces, respectively [19].

So far, LBM has rarely been applied in the context of battery simulations [26–29]. Only a few studies have been conducted in which LBM was applied to study electrolyte filling processes [30–33]. Jeon and co-workers [30–32] as well as Mohammadian and Zhang [34] studied the effect of structural properties and wettability on the filling duration. However, the underlying microstructures of the electrodes were rather simplified. Moreover, only 2D simulations were conducted to reduce the computational effort, although this reduces the number of available flow paths significantly and thereby strongly affects the saturation behavior, pore blocking, gas entrapment, and the accuracy of the results [27, 32]. Electrolyte filling of realistic 3D lithium-ion battery electrodes using LBM was investigated only recently by Shodiev *et al.* [33]. Their study focused on the correlation between the structural properties of electrodes and the filling duration. However, the wetting properties of active material and binder were assumed to be equal and the binder was fully solid and impermeable without considering its nanoporosity.

The present paper extends the findings of the aforementioned study [33]. In particular, the electrolyte filling process of realistic virtual 3D lithium-ion battery electrode structures is studied using LBM. Furthermore, motivated by the work of Pereira [35–37], MCSC is combined with a homogenization approach that is based on the grayscale (GS) or partial bounce-back (PBB) method [38]. This allows to simultaneously study the electrolyte flow in the mesoscopic pores confined by particles of the active material as well as in the nanoscopic pores of the binder phase without structurally resolving the latter. Note that our model is applied to simulate electrolyte wetting in lithium-ion battery cathodes but is not limited to this particular application. Other research fields which can benefit from this development are, e.g., flow phenomena in redox-flow batteries and fuel cells. Using our model, the process time as well as the influence of a wide range of relevant structural and physico-chemical properties of lithium-ion battery cathodes are studied. More precisely, the influence of the particle size distribution R_{PS}, the volume fraction ϕ_{A}, and the wettability θ_{A} of the active material on the filling process is investigated. In addition, a permeable binder is virtually added to some of the electrodes for which the inner volume fraction ϕ'_{B} and the wettability θ_{B} are varied.

This study aims to increase the understanding of the electrolyte filling process on the pore scale. It gives insight into the sensitivity of the aforementioned parameters on the pressure-saturation behavior during filling and the final degree of electrolyte saturation. In addition, for each of the electrodes it is shown which pressure profiles should be applied to achieve a steady and uniform filling process. Finally, also a detailed analysis is conducted regarding the amount and the size distribution of residual gas agglomerates that are entrapped during the filling process. It is shown how the residual gas phase can adversely affect the battery performance. Moreover, the efforts that are necessary to displace the gas agglomerates from the electrodes in a subsequent production step are quantified by computing permeabilities. All in all, the results presented here might be helpful to optimize the electrode and electrolyte design as well as the corresponding battery manufacturing step. The qualitative findings can also be used to optimize the filling process of anodes, separators or even other battery types.

The present paper is organized as follows. In Section 2 relevant aspects of LBM as well as the combination of MCSC and GS are described. The simulation setup is given in Section 3, where also the generation of the virtual electrode structures and the different analysis approaches are described. Section 4 gives an overview of the study including the range of influencing factors that were varied. The results are presented in Section 5. Finally, conclusions are drawn in Section 6.

2. Lattice Boltzmann Method

Details regarding the background, derivation, and implementation of LBM are described in the literature [17]. A brief overview of the fundamentals of LBM, MCSC [20], and GS [38] is given in the Supporting Information (cf. Section SI-1). In the following, the combination of MCSC with GS is described. It follows the approach developed by Pereira [35–37]. However, in contrast to the approach considered in [35–37], the Shan-Chen forcing approach is used and further adjustments with respect to the incorporation and weighting of interaction forces are made.

The MCSC can be used to model multi-phase flows. Interactions between the phases as well as the solid-fluid interactions with a solid wall are typically described as molecular interaction forces using a pseudopotential. The GS can be used to study physical situations in which the resolution of the numerical lattice is coarser than the smallest relevant physical length scale [39, 40], e.g. in fluid flow occurring simultaneously in pores with diameters differing by orders of magnitude. In the present work, MCSC and GS are combined to study the multi-phase flow of a liquid electrolyte and a gas phase in electrodes consisting of mesopores confined by the active material and nanopores within the binder.

2.1. Combining MCSC with GS

Similar to MCSC, in the model used for the simulations of the present work, each fluid component σ is represented by a distinct distribution function $\boldsymbol{f}^{\sigma}(\mathbf{x},t)$, where $\mathbf{x} \in \mathbb{R}^3$ and $t \geq 0$ denote the position of the lattice cell and the time, respectively. It is discretized in velocity space on a regular cubic 3D lattice. Each lattice cell is linked to its 18 nearest neighbors, resulting in the so-called D3Q19 velocity set (cf. Eq. (A.1)). The links correspond to the directions i along which the discrete distribution functions f_i are streamed.

The temporal evolution of $\boldsymbol{f}$ is described by the lattice Boltzmann equation (cf. Eq. (SI.1)). For the combined method, it reads

$$\begin{aligned} f_i^{\sigma}(\mathbf{x}+\mathbf{c}_i\Delta t, t+\Delta t) = \quad & (1-n_s^{\sigma}(\mathbf{x}))f_i^{\sigma}(\mathbf{x},t) \\ & -(1-n_s^{\sigma}(\mathbf{x}))\frac{\Delta t}{\tilde{\tau}^{\sigma}}\left(f_i^{\sigma}(\mathbf{x},t)-f_i^{\mathrm{eq},\sigma}(\mathbf{x},t)\right) \\ & +n_s^{\sigma}(\mathbf{x})f_{\bar{i}}^{\sigma}(\mathbf{x},t)\,. \end{aligned} \tag{1}$$

The second line of Eq. (1) describes the relaxation of $\boldsymbol{f}$ towards the Maxwell-Boltzmann equilibrium distribution function $\boldsymbol{f}^{\mathrm{eq}}$ (cf. Eq. (A.2)). The characteristic relaxation time is denoted by $\tilde{\tau}$ which is related to the kinematic viscosity via $\nu = c_s^2(\tilde{\tau} - 1/2)$. The parameter Δt is the time step. The third line of Eq. (1) is the bounce-back scheme (cf. [17]) representing no-slip conditions at solid walls [16, 19]. It corresponds to the state prior to the collision. The parameter $\bar{i}$ denotes the direction opposite to i. The only exception to this is the rest position $i = 0$, for which $i = \bar{i} = 0$.

Furthermore, in Eq. (1), $n_s \in [0,\, 1]$ is the solid fraction which comes from GS. It is a weighting factor that interpolates between fluidic (cf. lines 1 and 2 of Eq. (1)) and solid contributions (cf. line 3 of Eq. (1)) to $\boldsymbol{f}$ and can be used to describe homogenized regions consisting partially of pore space or fluid and partially of solid, such as the binder. In the extreme cases, for $n_s = 0$ or $n_s = 1$, Eq. (1) describes a purely fluid-like or a purely solid-like behavior, respectively.

From the moments of $\boldsymbol{f}$, different physical quantities such as the density or momentum can be determined (cf. Eqs. (A.3) & (A.4)). Due to MCSC any fluid or partially fluid lattice cell is computationally simultaneously occupied by both components. Under most conditions, a cell consists of a main component with the bulk density ρ and a dissolved component with the residual density $\rho_{\text{dis}} \ll \rho$.

Following MCSC, three types of forces are modeled. Those are the fluid-fluid interaction, the solid-fluid interaction, and external forces. The fluid-fluid interaction force $\boldsymbol{F}^{\sigma}_{\text{inter}}$ between the two components σ and $\bar{\sigma}$ is given by

$$\boldsymbol{F}^{\sigma}_{\text{inter}}\left(\mathbf{x}\right) = -\rho^{\sigma}\left(\mathbf{x}\right) G^{\sigma\bar{\sigma}}_{\text{inter}} \sum_{i} w_i \rho^{\bar{\sigma}}\left(\mathbf{x} + \mathbf{c}_i \Delta t\right) \mathbf{c}_i \Delta t, \tag{2}$$

where $G^{\sigma\bar{\sigma}}_{\text{inter}}$ is the interaction parameter that determines the strength of the cohesion and thereby also the interfacial tension. The lattice specific parameters w_i and $\mathbf{c}_i$ denote the weights and lattice velocities, respectively. Their numerical values are given in Appendix A.

The solid-fluid interaction force $\boldsymbol{F}^{\sigma}_{\text{ads}}$ which acts on the fluid component σ is given by

$$\boldsymbol{F}^{\sigma}_{\text{ads}}\left(\mathbf{x}\right) = -\rho^{\sigma}\left(\mathbf{x}\right) G^{\sigma}_{\text{ads}} \sum_{i} w_i s\left(\mathbf{x} + \mathbf{c}_i \Delta t\right) \mathbf{c}_i \Delta t, \tag{3}$$

where G^{σ}_{ads} is the interaction parameter which determines the wetting behavior. For the pure MCSC, i.e. for $n_s = 0$, it can be directly correlated with the contact angle θ [41] (cf. Eq. (A.6)). The function s serves as an indicator. Typically it is defined to be $s = 1$ at solid lattice points and $s = 0$ otherwise [42]. In this work and as also suggested by Pereira [35–37] it is chosen to be $s = n^{\sigma}_{s}$.

The external force $\boldsymbol{F}_{\text{ext}}$ contributing to each component is weighted by its density ratio

$$\boldsymbol{F}^{\sigma}_{\text{ext}} = \frac{\rho^{\sigma}}{\rho} F_{\text{ext}}, \tag{4}$$

where ρ^{σ} can be determined as is given by Eq. (A.3) and $\rho = \sum_{\sigma} \rho^{\sigma}$ is the total density.

The sum of the aforementioned force contributions (cf. Eqs. (2), (3) & (4)) scaled by the solid fraction determines the total force $\boldsymbol{F}^{\sigma}_{\text{tot}} = \left(\boldsymbol{F}^{\sigma}_{\text{inter}} + \boldsymbol{F}^{\sigma}_{\text{ads}}\right)/(1 - n^{\sigma}_{s}) + \boldsymbol{F}^{\sigma}_{\text{ext}}$ acting on a lattice cell. Combining the Shan-Chen forcing approach [17] with GS, $\boldsymbol{F}^{\sigma}_{\text{tot}}$ is finally incorporated as a force-induced contribution to the equilibrium velocity of each component

$$\mathbf{u}^{\text{eq},\sigma} = \frac{\sum_{\sigma} \rho^{\sigma} \mathbf{u}^{\sigma} / \tau^{\sigma}}{\sum_{\sigma} \rho^{\sigma} / \tau^{\sigma}} + (1 - n^{\sigma}_{s}) \frac{\tau^{\sigma} \boldsymbol{F}^{\sigma}_{tot}}{\rho^{\sigma}}. \tag{5}$$

The equilibrium velocity $\mathbf{u}^{\mathrm{eq},\sigma}$ determines $\boldsymbol{f}^{\mathrm{eq}}$ (cf. Eq. (A.2)). It must not be confused with the macroscopic streaming velocity $\mathbf{u}_{\mathrm{macro}}$ of the fluid mixture, which is given as

$$\mathbf{u}_{\mathrm{macro}} = \sum_{\sigma}(1 - n_s^{\sigma}) \left(\sum_i \frac{f_i^{\sigma}\mathbf{c}_i}{\rho^{\sigma}} + \frac{\boldsymbol{F}_{\mathrm{tot}}^{\sigma}\Delta t}{2\rho^{\sigma}} \right). \tag{6}$$

In comparison to the model proposed by Pereira [35–37], the current model uses the more common Shan-Chen forcing approach. Moreover, the redefinition of $\boldsymbol{F}_{\mathrm{tot}}^{\sigma}$ as described above cancels the scaling of the fluid-fluid and solid-fluid interaction forces in Eq. (5) and, thus, maintains a thin interface. For the model adaptions, the effect of the solid fraction n_s on the adhesive force $\boldsymbol{F}_{\mathrm{ads}}$ and the contact angle were determined. The results of which are given in the Supporting Information (cf. Section SI-2).

2.2. Model Parametrization

In porous media applications gravitational and viscous forces are typically negligible compared to capillary or surface forces [4, 18, 27, 43, 44]. Thus, the right parametrization of density and viscosity ratios between two components has only a minor effect on the physical results of the simulation [43, 44]. Therefore, and due to stability reasons of MCSC [18] the density and viscosity ratio is set to unity in the following. The other relevant model parameters and the corresponding conversion factors of the electrolyte-gas system studied here are given in Table 1 and Table 2, respectively.

All simulations conducted for this study have been carried out with an extended version of the open-source LBM tool *Palabos* (version 2.3) [45].

3. Simulation Setup

Artificially generated 3D lithium-ion battery cathode structures [46] were used as a geometrical basis for all simulations. Some of those structures were additionally infiltrated with a binder using a physically motivated algorithm as described in [47]. Recall that the focus of the present paper is twofold. First, the pressure-saturation behavior during the filling is studied. The obtained results allow to draw conclusions regarding the choice of the pressure profiles that should be applied to achieve a steady and uniform filling process. Second, the systems obtained at the end of the filling process are analyzed in detail. The main results of this analysis concern the final degree of electrolyte saturation, the size

Table 1: Overview of the physical quantities of the system consisting of electrolyte (E) and gas (G). Values are given in SI units and LBM units (lu: length unit; ts: time step; mu: mass unit). The asterisk indicates quantities in SI units.

	SI units	LBM units
density	$\rho^{\mathrm{E},*} = 1.20 \cdot 10^{3}\ \frac{\mathrm{kg}}{\mathrm{m}^3}$	$\rho^{\mathrm{E}} = 0.99\ \frac{\mathrm{mu}}{\mathrm{lu}^3}\ (\rho^{\mathrm{E}}_{\mathrm{dis}} = 0.01\ \frac{\mathrm{mu}}{\mathrm{lu}^3})$
	$\rho^{\mathrm{G},*} = 1.18\ \frac{\mathrm{kg}}{\mathrm{m}^3}$	$\rho^{\mathrm{G}} = 0.99\ \frac{\mathrm{mu}}{\mathrm{lu}^3}\ (\rho^{\mathrm{G}}_{\mathrm{dis}} = 0.01\ \frac{\mathrm{mu}}{\mathrm{lu}^3})$
kin. viscosity	$\nu^{\mathrm{E},*} = 2.314 \cdot 10^{-6}\ \frac{\mathrm{m}^2}{\mathrm{s}}$	$\nu^{\mathrm{E}} = 1.57 \cdot 10^{-5}\ \frac{\mathrm{lu}^2}{\mathrm{ts}}$
	$\nu^{\mathrm{G},*} = 1.57 \cdot 10^{-5}\ \frac{\mathrm{m}^2}{\mathrm{s}}$	$\nu^{\mathrm{G}} = 1.57 \cdot 10^{-5}\ \frac{\mathrm{lu}^2}{\mathrm{ts}}$
surface tension	$\gamma^{*} = 4.10 \cdot 10^{-2}\ \frac{\mathrm{kg}}{\mathrm{s}^2}$	$\gamma = 7.68 \cdot 10^{-2}\ \frac{\mathrm{mu}}{\mathrm{ts}^2}$
simulation		$\tilde{\tau}^{\mathrm{E}} = \tilde{\tau}^{\mathrm{G}} = 1.0$
parameters		$G^{\mathrm{EG}}_{\mathrm{inter}} = G^{\mathrm{GE}}_{\mathrm{inter}} = 1.75$
		$G^{\mathrm{G}}_{\mathrm{ads}} = -G^{\mathrm{E}}_{\mathrm{ads}} = \frac{1}{4} G^{\mathrm{EG}}_{\mathrm{inter}} (\rho^{\mathrm{E}} - \rho^{\mathrm{E}}_{\mathrm{dis}}) \cos\theta$

Table 2: Overview of the conversion factors between SI units and the corresponding LBM units (lu: length unit; ts: time step; mu: mass unit).

length	$C_l = 4.38 \cdot 10^{-7}\ \frac{\mathrm{m}}{\mathrm{lu}}$	time	$C_t = 1.3818 \cdot 10^{-8}\ \frac{\mathrm{s}}{\mathrm{ts}}$
mass	$C_m = 1.0194 \cdot 10^{-16}\ \frac{\mathrm{kg}}{\mathrm{mu}}$	pressure	$C_p = 1.2189 \cdot 10^{6}\ \frac{\mathrm{kg/m\ s}^2}{\mathrm{mu/lu\ ts}^2}$
kin. Viscosity	$C_\nu = 1.3884 \cdot 10^{-5}\ \frac{\mathrm{m}^2/\mathrm{s}}{\mathrm{lu}^2/\mathrm{ts}}$	force density	$C_f = 2.2941 \cdot 10^{9}\ \frac{\mathrm{m/s}^2}{\mathrm{lu/ts}^2}$

and spatial distribution of gas agglomerates being entrapped, and the permeability of the electrolyte and the gas in those partially saturated electrode structures. Moreover, it is shown how an imperfect filling might affect the battery performance. Details regarding the corresponding simulation setups and the analysis methods are given in the following.

3.1. Artificial Generation of Electrode Structures

The underlying cathode structures have been generated by means of the stochastic microstructure modeling framework which is described in [46]. It consists of three steps. First, a force-biased collective rearrangement algorithm is used to model the positions and sizes of active particles by a non-overlapping sphere packing [48, 49]. The packing density corresponds to the predefined volume fraction of active material and is varied in the range

$\phi_{\mathrm{A}} = \{0.5, 0.6, 0.7\}$ to obtain different electrode densities. Note that the radii of the spheres are drawn from a Gamma distribution, denoted by R_{PS}, with some shape and rate parameters $\alpha, \beta > 0$. More precisely, the following three cases are considered: Small spheres ($\alpha = 3.94$, $\beta = 2.17\, \mu m^{-1}$), medium spheres ($\alpha = 2.62$, $\beta = 1.05\, \mu m^{-1}$), and large spheres ($\alpha = 2.65$, $\beta = 0.75\, \mu m^{-1}$). The second modeling step involves a connectivity graph, which allows to additionally enforce connections between certain active particles, see [46]. However, in this study, the high volume fractions of active material already ensured a reasonable connectivity of active particles such that this modeling step was omitted, i.e., formally, an empty graph without any edges was used. In the third step, each sphere was replaced by a not necessarily spherical particle whose size and shape are described by means of a radius function. This function is represented by a truncated series expansion in terms of spherical harmonics [50], with the truncation parameter $L = 6$. The simulation of active particles represented in this way was carried out by means of Gaussian random fields on the sphere. The corresponding angular power spectrum is given by $a_1 = 0.65$, $a_2 = 4.13$, $a_3 = 0.82$, $a_4 = 0.31$, $a_5 = 0.17$, $a_6 = 0.11$, see [51] for details.

Finally, the system of simulated particles was discretized using a voxel size of $0.438\, \mu m$. In dependence on the volume fraction $\phi_{\mathrm{A}} = \{0.5, 0.6, 0.7\}$, the number of voxels was 82, 170, and $\{388, 323, 277\}$ along the x-, y-, and z-direction, respectively. Note that periodic boundary conditions in y- and z-direction were applied in all simulations. For the simulation scenarios with the IDs 9−14, a volume fraction of $\phi_{\mathrm{B}} = 0.21$ of the binder was added to the reference structure, i.e. ID 1 (cf. Table 3). Therefore, a morphological closing of the active material was applied where a sphere was used as the structuring element [52]. The radius of the sphere was chosen such that the predefined volume fraction of the binder was obtained.

3.2. Pressure-Saturation Behavior

The relationship between the capillary pressure and the saturation is an important measure for porous media applications. It can be used to predict which capillary pressure has to be overcome to reach a certain degree of saturation [53, 54]. A scheme of the simulation setup that was used to study the pressure-saturation behavior is shown in

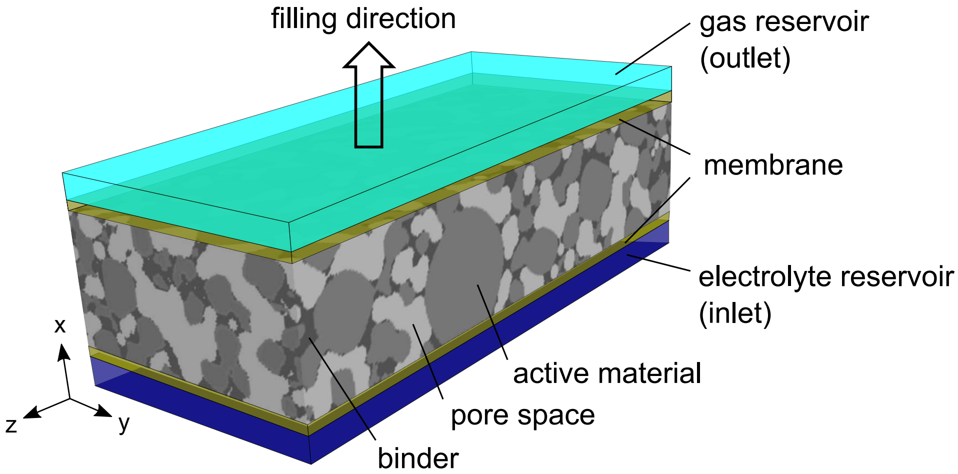

Figure 1: Scheme of the simulation setup. The electrode consists of active material (gray) and potentially a binder (darker gray) both enclosing the mesoscopic pore space (lighter gray). The reservoirs in which the densities of electrolyte and gas were prescribed are marked in blue and cyan, respectively. The membranes adjacent to the reservoirs are depicted in yellow. They were semi-permeable during the electrolyte filling process in $+x$-direction and impermeable during the permeability simulations in which a driving force was applied in $+y$-direction.

Figure 1. It is similar to setups that are typically used to study filling processes of porous media using LBM [39, 55]. The simulation system consists of the electrode structure as described in Section 3.1. The total pore space, i.e. the unification of the mesoscopic pores confined by the active material and the inner pores in the binder, was initially filled with a gas of density ρ^{G} and the dissolved electrolyte with density $\rho^{\mathrm{E}}_{\mathrm{dis}}$ (cf. Table 1).

Large scale simulations have been conducted. In dependence on the volume fraction of the active material $\phi_{\mathrm{A}} = \{0.5, 0.6, 0.7\}$, the total system sizes were $40\,\mu$m, $75\,\mu$m, and $\{170, 140, 120\}\,\mu$m along the x-, y-, and z-direction, respectively. This corresponds to simulation domains of up to 5.9 million lattice cells. The simulations were computationally expensive and, thus, conducted on the supercomputers JUSTUS 2 and Hawk using more than 500 cores in parallel execution.

Periodic boundary conditions were applied along the y- and z-direction. This is in accordance with the periodicity of the electrode structures. Along the x-direction an electrolyte reservoir was added at the inlet, and an gas reservoir was added at the outlet. The reservoirs had a thickness of four layers each. They had the purpose to prescribe the density of the corresponding fluid which is directly proportional to the pressure in LBM simulations (cf. Eq. (A.5)). At the inlet the electrolyte density was initially set to ρ^{E} (and the gas density to $\rho^{\mathrm{G}}_{\mathrm{dis}}$). During the simulation run, ρ^{E} at the inlet was incrementally increased over time. The density increments were determined using a control loop under the condition of steady and uniform filling with a predefined target saturation rate. At the outlet the gas density was kept constant at the initial value ρ^{G} (and the electrolyte density at $\rho^{\mathrm{E}}_{\mathrm{dis}}$). Each reservoir was divided from the electrode by a semi-permeable membrane to prevent a breakthrough of one of the two fluid components. The membrane at the inlet was permeable for the electrolyte only whereas he membrane at the outlet was permeable for the gas only. The impermeability was implemented by applying the bounce-back scheme (cf. [17]) to the non-permeating fluid component.

From the simulations the pressure difference Δp was determined as

$$\Delta p = \langle p \rangle_{\mathrm{inlet}} - \langle p \rangle_{\mathrm{outlet}}\,, \tag{7}$$

where p was evaluated using Eq. (A.5), and $\langle p \rangle$ denotes the average pressure in the inlet and outlet reservoirs. The pressure difference Δp is directly related to the capillary pressure p_c as $p_c = p_0 - \Delta p$, where p_0 is the absolute capillary pressure at zero electrolyte saturation ($p_0 = p_c(S^{\mathrm{E}} = 0)$). In the current work, Δp was chosen over p_c to ensure that all pressure-saturation curves start from the same value $\Delta p(S^{\mathrm{E}} = 0) = 0$. This improves the comparability between the different simulations.

The electrolyte saturation S^{E} is defined as

$$S^{\mathrm{E}} = \frac{N_{\mathrm{pore}}(\rho^{\mathrm{E}} \geq 0.5) + (1 - n_s) N_{\mathrm{binder}}(\rho^{\mathrm{E}} \geq 0.5)}{N_{\mathrm{pore}} + (1 - n_s) N_{\mathrm{binder}}}, \tag{8}$$

where the denominator and numerator correspond to the total pore space and the pore space in which $\rho^{\mathrm{E}} \geq 0.5$ mu/lu^3, respectively. The number of pore lattice cells in the electrode structures and the binder are denoted by N_{pore} and N_{binder}, respectively. The latter are multiplied by the effective nanoscopic pore volume $(1 - n_s) = (1 - \phi'_{\mathrm{B}})$. Note, that for the calculation of the saturation only the lattice cells between the two membranes were considered.

A simulation run consisted of approximately 1,000,000 time steps. Only the two simulations in which the process time was varied by the factor 0.5 and 2, accordingly consisted of approximately 500,000 and 2,000,000 time steps. The pressure difference and the saturation were determined every 10,000 time steps during the production run. The simulations were stopped when a further saturation of the electrode was not possible and led to a strongly divergent pressure at the inlet and a steep increase of Δp. The corresponding distribution functions of both fluids were recorded. They represent the state of the system at the end of the filling process and were used for further data analysis and as input for subsequent permeability simulations.

The statistical uncertainty of the pressure-saturation curves was estimated for a representative electrode structure. In addition, also the bias, the average absolute deviation (AAD), and the maximum deviation were determined. The mean standard deviation of the average curve was $2-4\,\mathrm{kPa}$ for Δp and to $0.75\,\%$ for S^{E}. The detailed results are given in the Supporting Information (cf. Section SI-3).

3.3. Gas Entrapment

As was recently reported by Sauter *et al.* [11], gas entrapment can significantly reduce effective ionic conductivities in separators. The gas phase is a poor conductor that hinders ion transport, blocks transport pathways, and reduces the connectivity of the electrolyte phase. This can be quantified by the mean geodesic tortuosity, which is a geometric characteristic that is of great importance with respect to transport processes [56, 57]. In general, one considers the lengths of shortest paths, which have to be completely contained in a predefined phase, from a starting plane to a target plane. In this study, the shortest paths from the inlet to the outlet are computed using Dijkstra's algorithm [58]. By dividing the lengths of those shortest paths by the thickness of the electrode in x-direction (i.e. the distance between the inlet and the outlet) and by subsequent averaging over all starting points in the inlet, an estimator of the mean geodesic tortuosity is obtained. For a more formal introduction to geodesic tortuosity, see [59].

Two different geodesic tortuosities are determined, i.e. τ_0 and τ_{end}. For τ_0, the active material and partially also the binder are considered as obstacles for the ionic transport. Thus, τ_0 represents the geodesic tortuosity for an ideal case in which each pore contributes to the ionic pathways. In contrast, τ_{end} is the geodesic tortuosity at the end of the filling process. Then, also entrapped gas is an obstacle, where a voxel belongs to the gas phase if its density exceeds $\rho^{\mathrm{G}} \geq 0.5$. In case of simulations with binder (IDs 9-14), an additional weighting factor w_{B} is introduced for the binder. It depends on the inner volume fraction of the binder ϕ'_{B} via the Bruggeman relation [60] and accounts for the increased path length within a binder voxel. More precisely, the equation $w_{\mathrm{B}} = \phi'^{-0.5}_{\mathrm{B}}$ is used, which corresponds to the frequently used Bruggeman exponent of -0.5 [61, 62].

In addition, gas that accumulates at the surface of active material reduces the electrochemically active surface area and, thereby, limits the lithiation process. Thus, the surface area of active material that is blocked by gas agglomerates is also analyzed. For this purpose, the surface area of active material (S_{A}), gas (S_{G}) and the union of active material and gas ($S_{\mathrm{A\cup G}}$) is estimated from voxelized image data by means of differently weighted local $2 \times 2 \times 2$ voxel configurations, using the weights proposed in [63]. This allows to compute the fraction $S_{\mathrm{A\cap G}}$ of blocked active material surface, which is given by

$$S_{\mathrm{A\cap G}} = \frac{S_{\mathrm{A}} + S_{\mathrm{G}} - S_{\mathrm{A\cup G}}}{2S_{\mathrm{A}}} \in [0,\, 1]. \tag{9}$$

Note that the interfacial area between active material and gas contributes to S_{A} and S_{G} but not to $S_{\mathrm{A\cup G}}$, which leads to the factor of 2 in the denominator.

3.4. Permeability

The permeability k is a measure for the ability of a porous medium to perfuse a fluid flow. Thus, it is a measure for the fluid mobility. In this study, the permeability is used to quantify the effort that is necessary for displacing entrapped gas agglomerates from electrodes.

The simulation setup that was used to determine the permeability is similar to the setup in Section 3.2. In the following only the deviations from this setup are described. The permeability simulations were initialized with an electrolyte and gas distribution identical to the ones at the end of the filling process. Periodic boundary conditions were applied along all directions. The membranes were fully impermeable to conserve the fluid composition within the electrode structure. Also the densities of both components were constant. Along the positive y-direction the external force density $\mathsf{f}_y = 5 \cdot 10^{-4}\,\mathrm{lu/ts^2}$ was applied to both fluids and to each lattice cell that contained fluid. The magnitude of f_y was in a suitable range such that the momentum showed a linear relationship with the external force [42, 44, 64]. For the permeability analysis only the lattice cells between the two membranes were considered, i.e. reservoirs were excluded.

From the simulations the permeability k_y^σ of the component σ along the y-direction was determined as

$$k_y^\sigma = \frac{u_{\mathrm{Darcy},y}^\sigma \nu^\sigma}{\mathsf{f}_y}. \tag{10}$$

Thus, k_y^{E} and k_y^{G} denote the permeabilities of the electrolyte and the residual gas phase, respectively. While ν and f_y were input parameters to the simulations, the Darcy velocity $u_{\mathrm{Darcy},y}^\sigma$ of the σ-component in y-direction was determined from the simulations as

$$u_{\mathrm{Darcy},y}^\sigma = \frac{\sum_j^{N_{\sigma,\mathrm{bulk}}} u_y^\sigma(x_j)}{N_{\mathrm{total}}}. \tag{11}$$

The Darcy velocity is the sum of the velocity component in the y-direction, u_y, over all lattice cells $j \in N_{\sigma,\mathrm{bulk}}$ that belong to the bulk phase of the σ-component $N_{\sigma,\mathrm{bulk}}$, divided by the total number of lattice cells N_{total}. The bulk phase was defined such that all fluid lattice cells directly adjacent to a solid surface, i.e. connected via the lattice links, were excluded. Moreover, only lattice points in which the dissolved density of the complementary $\bar{\sigma}$-component, $\rho_{\mathrm{dis}}^{\bar{\sigma}}$, was below $0.2\,\mathrm{mu/lu}^3$ were considered as bulk phase. This reduces errors from spurious currents occurring at the fluid-fluid and solid-fluid interfaces [18, 43].

Each simulation consisted of two parts. Initially 100,000 time steps were performed in which a steady state was established. Subsequently, a production run of 100,000 time steps was conducted. The permeability was determined every 1,000 time steps during the production run. Therefrom, the uncertainty of the permeability was determined as the standard deviation of the time-averaged values.

4. Overview of the Study

The influencing factors on the electrolyte filling process that are considered in this study are: the filling speed which corresponds to the process time t_{P}, the particle size distribution R_{PS}, the volume fraction ϕ_{A}, and the wettability θ_{A} of the active material, as well as the inner volume fraction ϕ'_{B} and wettability θ_{B} of the binder. The volume fraction ϕ_{A} is the number of active material lattice cells divided by the total number of lattice cells in the system. In contrast, the inner volume fraction ϕ'_{B} is not a system wide parameter, but describes the volume fraction of solid binder material within a single binder lattice cell. For this study, it was assumed that the physical and numerical values correspond directly, $\phi'_{\mathrm{B}} = n_s$, which is a simplification and not generally true [37, 38].

An overview of the simulations from the current work is given in Table 3. To determine the pressure-saturation behavior, 16 large-scale 3D simulations were conducted. Another 16 simulations were conducted to determine the electrolyte permeability at the end of the filling process. The material properties of the active material (IDs 1−8) and the binder (IDs 9−14) were varied. For all aforementioned simulations, i.e. IDs 1−14, the target saturation rate was identical. It was chosen to reach complete filling within 1,000,000 time steps, i.e. $t_{\mathrm{end}} = 1.378 \cdot 10^{-2}\,\mathrm{s}$. Note that the process duration is short as the electrode volume is in the $\mu\mathrm{m}^3$-range. The IDs 15 and 16 refer to simulations in which the process time was varied. Therefore, compared to the previous value, the target saturation rate was halved for ID 15 and doubled for ID 16.

Two simulations were used as reference, where all parameters were chosen such that they were in the middle of the parametric ranges studied in this work. Unless specified otherwise, subsequent simulations use those default parameters. The default simulation without binder is denoted as ID 1 (cf. first column in Table 3). The default simulation with binder is denoted as ID 9.

Starting from ID 1, all influencing factors concerning the active material were studied independently. The parameters R_{PS}, ϕ_{A}, and θ_{A} were varied separately, while the other influencing factors were kept constant at their default values. The influence of the binder was studied by separately varying ϕ'_{B} or θ_{B}, while keeping all other influencing factors constant at the values identical to those from ID 1. The structural properties of the IDs 15 and 16 were identical to those of ID 1.

Filling and permeability simulations were conducted for each ID. Some numerical results of the simulations are also given in Table 3.

5. Results and Discussion

The numerical results of the entire data set presented in this section are given in the Supporting Information (cf. Section SI-4).

Table 3: Overview of the performed simulations. The default simulation without binder is ID 1. The default simulation with binder is ID 9, where the properties of the active material were identical to those of ID 1. The simulations 1−8, 15, and 16 did not contain any binder and thus are marked by '−' in columns 5 and 6. In contrast, the simulations 9−14 contained binder. Plain entries of settings have the same value as ID 1 or 9, respectively. Beside the total duration of the filling process t_{end}, also the results of the final saturation $S^{\mathrm{E}}_{\mathrm{final}} = S^{\mathrm{E}}(t_{\mathrm{end}})$, as well as the permeability of the electrolyte k^{E}_{y} and the residual gas phase k^{G}_{y} are given.

sim. ID	R_{PS}	ϕ_{A}	θ_{A} (°)	ϕ'_{B}	θ_{B} (°)	t_{end} (10^{-2} s)	$S^{\mathrm{E}}_{\mathrm{final}}$ (%)	k^{E}_{y} (10^{-15} m^2)	k^{G}_{y} (10^{-15} m^2)
1	medium	0.6	90	−	−	1.46	89.6	91.72	9.62
2	small			−	−	1.41	90.7	102.58	10.55
3	large			−	−	1.52	95.3	198.66	70.64
4		0.7		−	−	1.26	79.1	32.28	5.82
5		0.5		−	−	1.48	95.6	264.33	97.59
6			60	−	−	1.48	96.8	88.98	40.97
7			80	−	−	1.48	92.7	92.16	16.38
8			100	−	−	1.42	86.1	91.64	9.66
9	medium	0.6	90	0.5	60	1.39	95.9	9.82	1.00
10				0.6		1.39	95.5	7.21	1.06
11				0.4		1.38	95.3	13.19	1.64
12					30	1.35	96.6	10.03	5.93
13					90	1.35	89.1	8.80	1.75
14					120	1.02	63.0	4.99	1.89
15	medium	0.6	90	−	−	2.98	90.1	92.21	8.11
16	medium	0.6	90	−	−	0.73	89.3	91.30	10.63

5.1. Pressure-Saturation Behavior

Figures 2 and 3 show the pressure-saturation curves of all simulations from this study. All curves follow a sigmoidal behavior with steep sides for low and high electrolyte saturation, and an almost horizontal regime for medium saturations. This trend can be explained by the Young–Laplace equation ($p_c = 2\gamma/R$) which describes the inverse proportionality between the capillary pressure p_c and the pore radius R. At the beginning, when electrolyte invades the electrode, also smaller pores at the inlet need to get passed. This leads to a strong increase in Δp. Thereafter, a flat plateau-like value is reached, during which large parts of the electrode are filled through larger pores primarily. Finally, to reach a high saturation, also smaller pores have to be filled, leading to a strong increase in Δp again. For all cases, the initial saturation $S^{\mathrm{E}}_{\mathrm{init}}$ deviates from zero. This means that electrolyte invades the electrode without increasing Δp in the simulations. Also the final saturation $S^{\mathrm{E}}_{\mathrm{final}}$ for all cases deviates from the theoretical optimum of 100 %. This is related to gas agglomerates being entrapped in the pore space and has already been reported numerously in the literature [3, 4, 11, 15, 19, 33, 39, 43, 65].

Figure 2 shows the results for the influencing factors that are purely related to the active material as well as the process time. In contrast, Figure 3 shows the results for the influencing factors that are purely related to the binder. In Figures 2 and 3 and all other figures in the following, the influencing factors are indicated by the colors. The line types correspond to a specific value of the corresponding influencing factor. In Figure 2, the result of ID 1 is depicted by the blue solid line. In Figure 3, the result of ID 9 is depicted by the purple solid line. Both serve as reference for the following analysis.

Figure 2 a) & b) show the influence of the particle size distribution R_{PS} and the volume fraction ϕ_{A} of the active material. Significant differences are observed. Compared to the reference case, larger particle sizes (ID 3) and a smaller volume fraction of the active material (ID 5) result in a smaller Δp and an increased final saturation $S^{\mathrm{E}}_{\mathrm{final}}$. Both are directly connected to larger pore sizes and thus a reduced Δp. The contrary is observed for a larger active material volume fraction (ID 4) which facilitates gas entrapping.

The influence of the wetting behavior of the active material is shown in Figure 2 c). The results clearly indicate that decreasing the contact angle θ_{A} and thereby increasing the wettability reduces Δp and leads to a better final degree of saturation.

Figure 2 d) shows that the influence of the filling speed or the process time t_{P} on the pressure-saturation behavior is low for the range of values studied here. There is almost no difference between a medium (ID 1) and slow filling (ID 15). Thus, both processes were slow enough such that the capillary forces dominated the viscous forces. In contrast, for a faster filling (ID 16), viscous effect becomes more apparent [43, 66]. The flow regime then tends to transition from capillary fingering to viscous fingering which leads to more gas entrapment [66, 67].

Figure 3 a) & b) show the influence of the binder on pressure-saturation curves. In general, the presence of the binder shifted $S^{\mathrm{E}}_{\mathrm{init}}$ to larger values. This was partially due to the definition of the saturation (cf. Eq. (8)), where adding a solid binder reduces the total pore space. This effect was even more pronounced for stronger wettabilities which induce a faster percolation.

The inner volume fraction of the binder in the range of the values studied here, has only a minor effect on the pressure-saturation behavior. This is different for the binder wettability. Using a binder that has a better wettability than the active material (IDs 9−12) decreases Δp, enhances the electrolyte percolation, increases $S^{\mathrm{E}}_{\mathrm{init}}$, and leads to a better final saturation of the electrode. In contrast, adding a neutrally wetting (ID 13) or dewetting binder (ID 14) to the electrode has negative effects. Larger Δp are necessary to drive the flow. Moreover, a dewetting binder leads to effects similar to pore clogging. It prevents electrolyte percolating into the binder and entraps large amounts of residual gas in the binder structure and at its surface.

5.2. Total Duration of the Filling Process

The saturation-time behavior for different process times or target saturation rates is given in Figure 4. The results show a similar qualitative behavior. The control function adjusts the inlet density increment such that a steady and uniform filling process is achieved. This is shown by the almost linear behavior of the saturation-time curves over wide ranges of the simulation. Deviations from that behavior occur at the beginning and the end of the simulations, where Δp is highly sensitive to the saturation (cf. Figure 3).

As both a fast filling and a low final saturation decrease t_{end}, a relative measure, i.e. the reciprocal filling rate

$$\tilde{t}_{\mathrm{end}} = \frac{t_{\mathrm{end}}}{S^{E}_{\mathrm{final}}}, \tag{12}$$

is introduced. It corresponds to the average time needed to fill 1 % of the electrode's pore space.

For the IDs 1−14, the target saturation rate and the targeted reciprocal filling rate were identical ($\tilde{t}_{\mathrm{target,end}} = 1.378 \cdot 10^{-4}\,\mathrm{s}/\% - \Delta S^{E}$). However, the actual values for $\tilde{t}_{\mathrm{end}}$

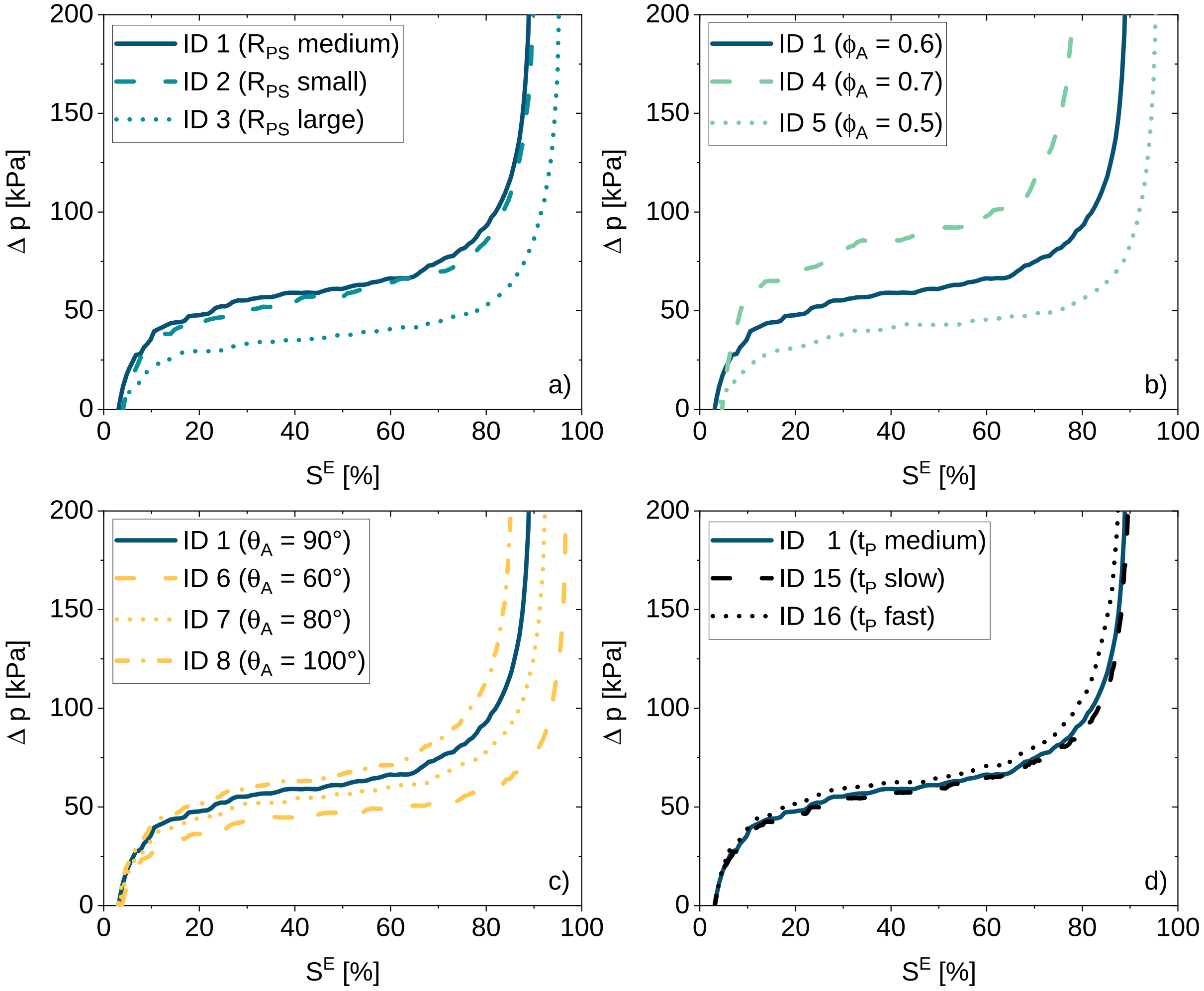

Figure 2: Pressure-saturation behavior of electrodes without binder. ID 1 is depicted with the blue solid line. The influencing factors are indicated by the colors. Those are a) the particle size distribution R_{PS} (turquoise), b) the volume fraction of the active material ϕ_{A} (green), c) the wettability θ_{A} (orange), and d) the process time t_{P} (black). The line types correspond to a specific value of the influencing factor.

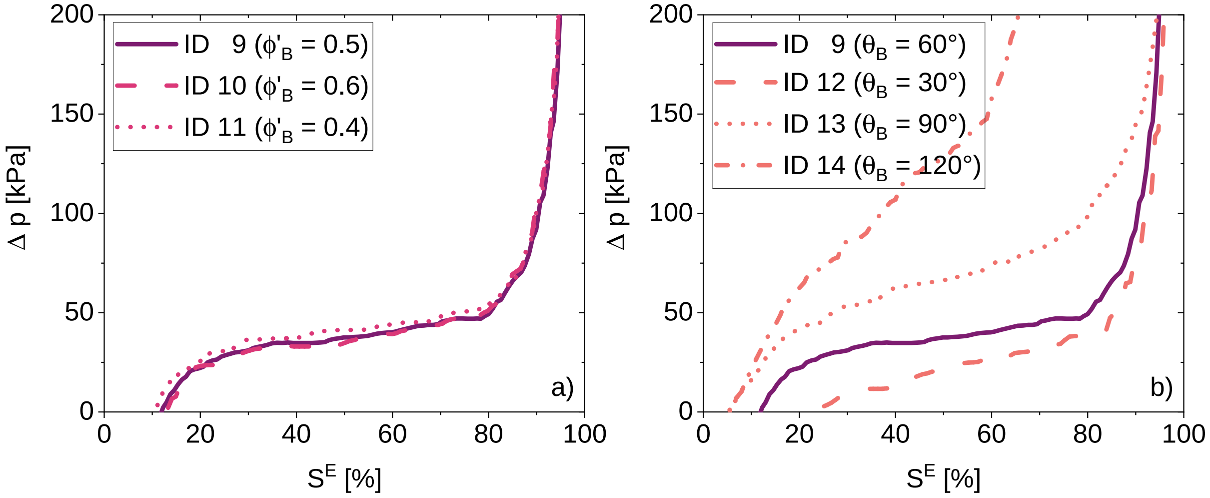

Figure 3: Pressure-saturation behavior of electrodes with binder. ID 9 is depicted with the purple solid line. The influencing factors are indicated by the colors. Those are a) the inner volume fraction of the binder ϕ'_{B} (magenta), and b) the wettability θ_{B} (red). The line types correspond to a specific value of the influencing factor.

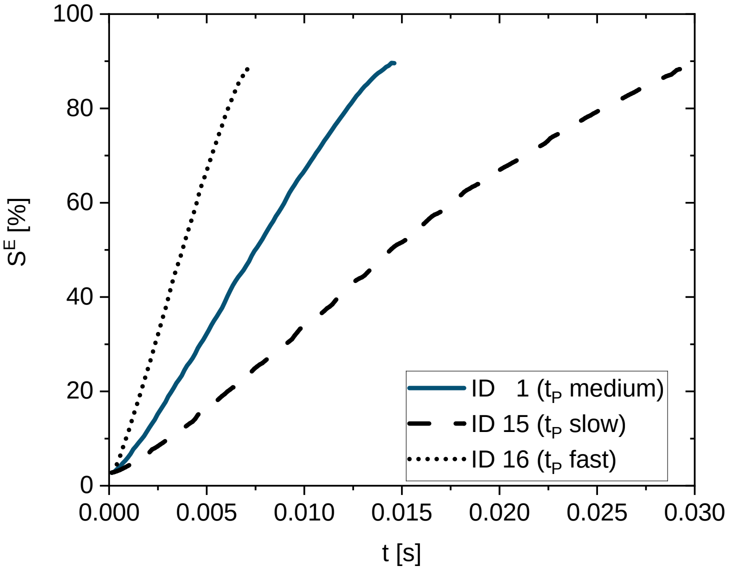

Figure 4: Saturation-time behavior for the reference electrode without binder. Results are shown for three processing times: ID 1 (t_{P} = medium, blue solid line), ID 15 (t_{P} = slow, black dashed line), and ID 16 (t_{P} = fast, black dotted line).

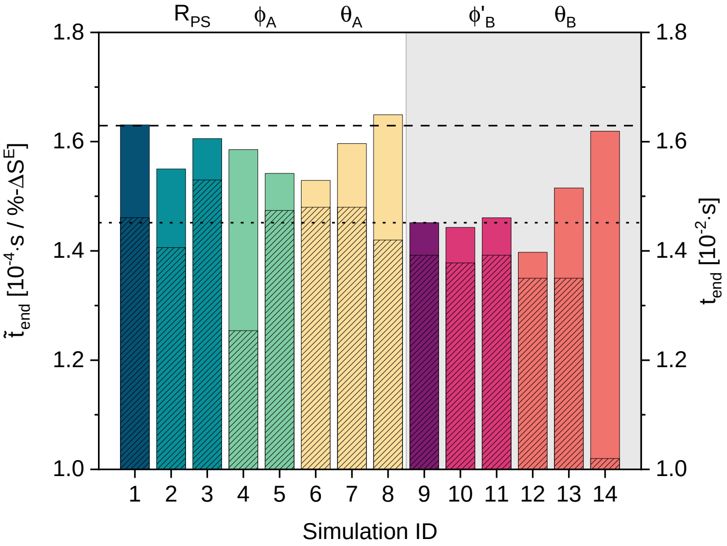

Figure 5: Overview of the reciprocal filling rate $\tilde{t}_{\mathrm{end}}$ and the total duration of the filling process t_{end}. The values of $\tilde{t}_{\mathrm{end}}$ are depicted with the colored bars and related to the left ordinate axis. The values of t_{end} are depicted with the hatched bars and related to the right ordinate axis. The influencing factors are indicated by the colors. The corresponding simulation IDs are given at the abscissa. Simulations of electrodes with binder are highlighted by the gray background. The horizontal dashed and dotted lines represent $\tilde{t}_{\mathrm{end}}$ of ID 1 and ID 9, respectively.

deviated from the target values due to the effect of the physico-chemical influencing factors on the control function of the inlet boundary condition.

For the IDs 1−14, the results of t_{end} and $\tilde{t}_{\mathrm{end}}$ are shown in Figure 5. There is a clear correlation between t_{end} and the structural properties of the active material (IDs 1−5). The smaller the pores are, the shorter is the total duration of the filling process. This is different for $\tilde{t}_{\mathrm{end}}$ where the values scatters without any clear influence. The wettability of the active material (IDs 6−8) shows a contrary effect. Here, t_{end} is hardly affected by θ_{A}. However, a stronger wettability results in a lower reciprocal filling rate and, thus, a shorter filling process. The same effect is observed for the binder wettability (IDs 9, 12−14) and has also been reported in the literature [12, 30, 68]. Moreover, the filling of electrodes with binder is about 20 % faster compared to electrodes without binder. However, as mentioned before, this is also related to the reduction of the total pore space, when adding a binder.

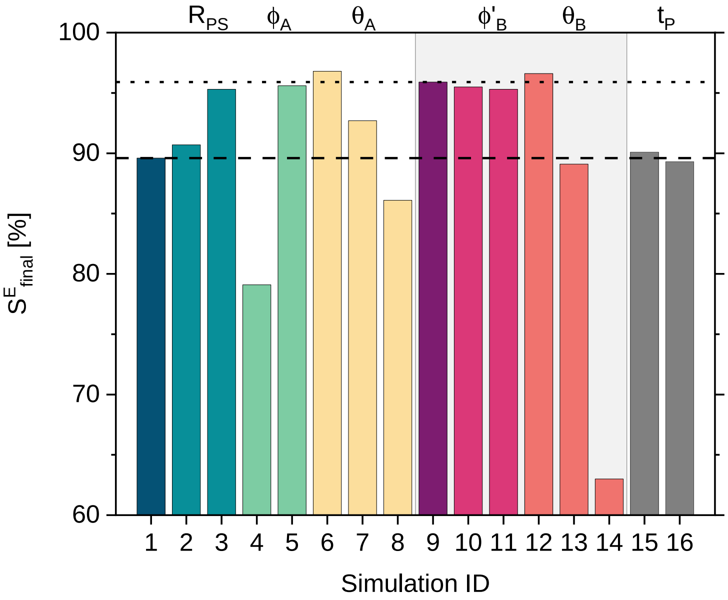

Figure 6: Overview of the final saturation of the filling process S^{E}_{final}. The meaning of the colors is identical to those from Figure 5. The horizontal dashed and dotted lines represent $S^{\mathrm{E}}_{\mathrm{final}}$ of ID 1 and ID 9, respectively.

5.3. Final Saturation and Gas Entrapment

First, the final saturations at the end of the filling process are compared. The numerical values of $S^{\mathrm{E}}_{\mathrm{final}}$ are listed in Table 3 and shown in Figure 6.

The final saturations are in a broad range $S^{\mathrm{E}}_{\mathrm{final}} = [63.0, 96.8]\,\%$ which corresponds to a residual gas volume fraction of $[37.0, 3.2]\,\%$. Most of the electrodes are filled to an extent of 90 % and more. Compared to ID 1 a larger degree of saturation is observed for electrodes with 1) larger pores, i.e. a larger particle size distribution (ID 3) or a smaller volume fraction of the active material (ID 5), 2) better surface wettability (IDs 6 and 7), and 3) in the presence of a hydrophilic binder (IDs 9−12). In contrast, incomplete filling correlates with 1) small pores, i.e. a large volume fraction of the active material (ID 4), and 2) hydrophobic surfaces of the active material (ID 8) and the binder (ID 14). These general findings agree with findings from experimental [2, 9, 11, 12, 54] and simulative [30, 32–34, 54, 68] studies in the literature.

Figure 7 shows qualitative and quantitative information of the gas agglomerates for the two reference cases. The amount of residual gas phase is 10.4 % in Figure 7 a) and 4.1 % in Figure 7 b). In the top figure, the gas entrapment is shown qualitatively. There, gas agglomerates are depicted in gray. All other components are fully transparent. In the middle figure, a cross section through the xy-plane at $z = 200\,\text{lu}$ is shown. There, the active material is depicted in black, the binder is depicted in gray, and the gas phase is depicted in red or orange in regions with or without binder, respectively. In the bottom figure, the corresponding size distributions of the gas agglomerates are given. They show the ratio of the cumulated gas volume V^{G} to the total pore volume $V^{\mathrm{E+G}}$ as a function of the equivalent gas bubble radius $R_{\mathrm{eq}}^{\mathrm{G}}$.

The top row of Figure 7 shows that more gas phase is entrapped in the electrode of ID 1 compared to ID 9. Moreover, for ID 1, the gas agglomerates are also larger. Note that more gas phase was entrapped close to the inlet. This can also be observed from the middle row of Figure 7 where most of the gas phase agglomerates in the lower half of the figure, which is closer to the inlet. For ID 1, the gas agglomerates are mainly entrapped in small pores and corners confined by the active material. The location of the gas agglomerates is almost the same for ID 9. However, since the binder has a better wettability than the active material the gas agglomerates are smaller. These results are supported by the quantitative plot at the bottom row of Figure 7. The plots show a similar behavior for small gas agglomerates with $R_{\mathrm{eq}}^{\mathrm{G}} < 5\,\text{lu}$. However, both plots differ for larger $R_{\mathrm{eq}}^{\mathrm{G}}$. A broad range of medium and large gas agglomerates up to $R_{\mathrm{eq}}^{\mathrm{G}} = 14\,\text{lu}$ is observed for ID 1. In contrast, for ID 9, almost all agglomerates are smaller than $R_{\mathrm{eq}}^{\mathrm{G}} = 5\,\text{lu}$.

The corresponding size distributions of the remaining simulations, i.e. IDs 2−8 and IDs 10−16, are given in the Supporting Information (cf. Figures SI-3 and SI-4). The most relevant findings of which are summarized in the following: 1) For almost all influencing factors , the slope $\Delta\left(V^{\mathrm{G}}/V^{\mathrm{E+G}}\right)/\Delta R_{\mathrm{eq}}^{\mathrm{G}}$ is similar over wide ranges of $R_{\mathrm{eq}}^{\mathrm{G}}$ until the asymptotic end value of $V^{\mathrm{G}}/V^{\mathrm{E+G}}$ is being approached. This indicates a similar gas entrapment for small and medium gas agglomerates up to the asymptotic value amongst all structures. 2) A larger volume fraction of the active material and smaller pores lead to larger gas agglomerates and a better connectivity of the gas phase. 3) A strong wettability of both the active material and the binder leads to less gas entrapment and remarkably smaller gas agglomerates. 4) There is only a small influence of the process time on the size distribution of gas agglomerates. Applying a fast filling speed (ID 16) leads to the formation of more medium-sized gas agglomerates.

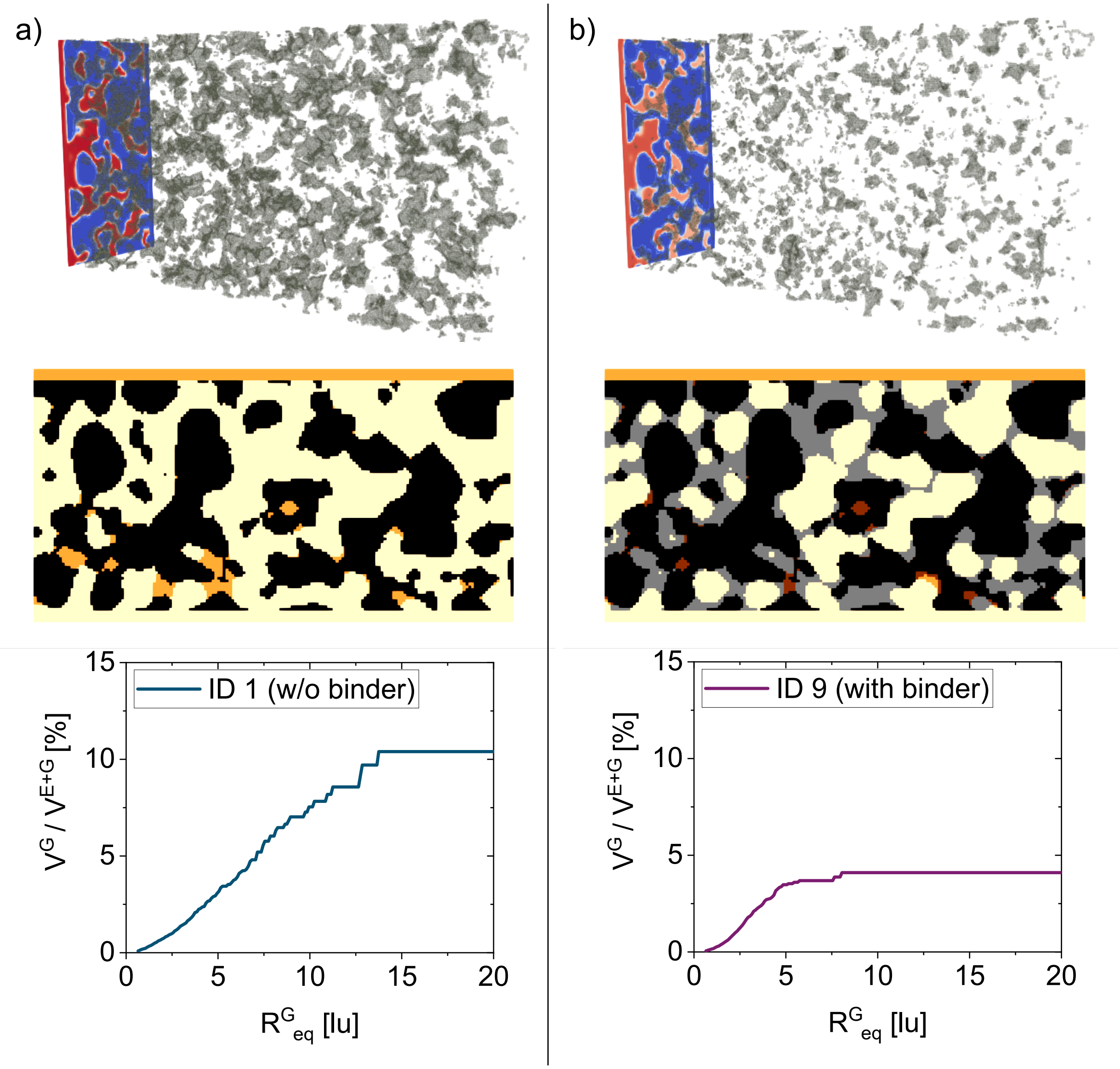

Figure 7: Comparison of the gas entrapment for the two reference simulations: a) ID 1 with 10.4 % residual gas phase and b) ID 9 with 4.1 % residual gas phase. Top: Visualization of the residual gas phase being entrapped in the electrodes at the end of the filling process. The gas phase is depicted in gray. The electrolyte and the solid components are fully transparent. Middle: Cross section through the xy-plane at $z = 200\,\mathrm{lu}$. The active material is depicted in black, the binder is depicted in gray, and the gas phase is depicted in red or orange in regions with or without binder, respectively. Bottom: Size distributions of gas agglomerates. The ratio of the cumulated gas volume V^{G} to the total pore volume $V^{\mathrm{E+G}}$ is shown as a function of the equivalent gas bubble radius $R^{\mathrm{G}}_{\mathrm{eq}}$.

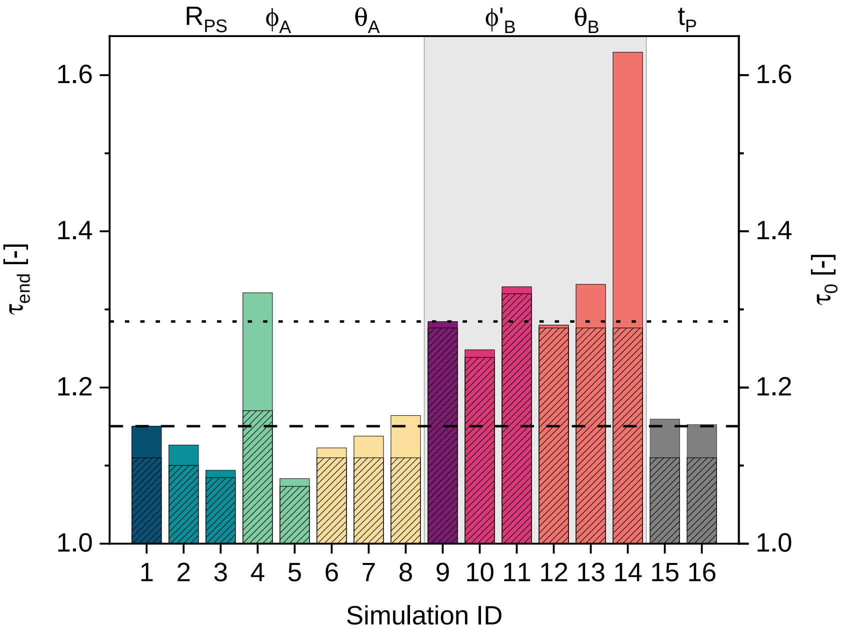

Figure 8: Overview of geodesic tortuosities τ_0 and τ_{end}. The values of τ_{end} are depicted with the colored bars and related to the left ordinate axis. The values of τ_0 are depicted with the hatched bars and related to the right ordinate axis. The meaning of the colors and line types is similar to those from Figure 5.

The residual gas phase with its low ionic conductivity, is known to have a twofold impact on the battery performance [3–6, 11, 33]. Gas agglomerates inhibit the ion transport, leading to longer transport pathways, and thereby decreasing the effective ionic conductivity. In addition, the gas prevents ion transport to the surface of the active material, reducing the electrochemically active surface area available, thus, increasing overpotentials, and reducing the specific battery capacity.

The influence on the geodesic tortuosities as a measure for the effective conductivity is shown in Figure 8. The binder leads to a tortuosity increase of approximately 10 %. When comparing the results of τ_{end} with the corresponding final saturation (cf. Figure 6), both behave inversely proportional. Thus, the transport pathways are longer the more gas agglomerates are entrapped. For most of the electrodes for which $S^{\text{E}}_{\text{final}} > 90\,\%$ the influence is only minor. However, in the extreme case (ID 14) the shortest pathway increases tremendously by 27.7 %.

The influence of the entrapped gas phase on the extent of the electrochemically active surface area $A_{\text{A,act}}$ is shown in Figure 9. As expected a direct proportionality of $A_{\text{A,act}}$ and $S^{\text{E}}_{\text{final}}$ is observed. A better saturation and less residual gas phase lead to more active

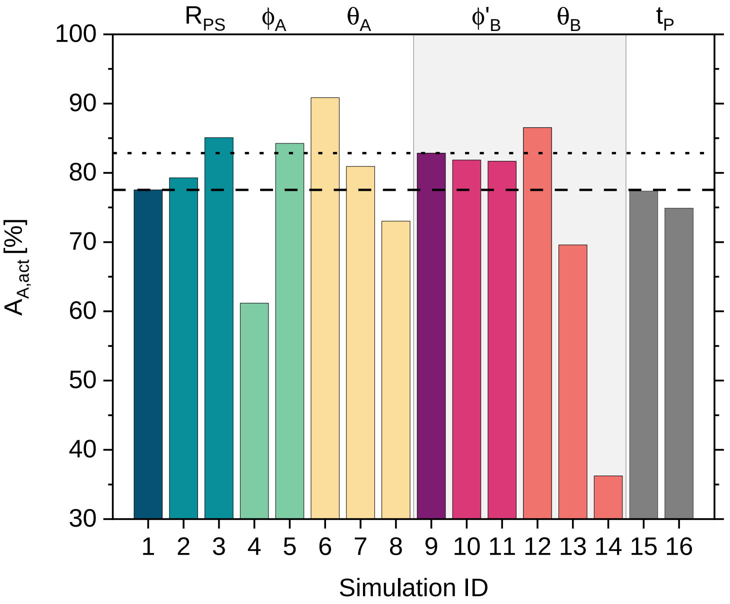

Figure 9: Overview of the ratio of the electrochemically active surface area $A_{\mathrm{A,active}}$. The meaning of the colors is identical to those from Figure 5. The horizontal dashed and dotted line represent $A_{\mathrm{A,act}}$ of ID 1 and ID 9, respectively.

material being in direct contact to the electrolyte. However, the quantities of the results are surprising. Even for the best saturation (ID 6) and a strongly hydrophilic, i.e. gas repelling, surface, about 9 % of the total active surface area are passivated by gas phase. For the worst case (ID 14) even 63.8 % of active surface area are blocked.

Note that these results represent the gas entrapment right after the filling. It might differ from the amount of gas entrapment at the end of the whole manufacturing process during which gas is typically removed in subsequent production steps.

The aforementioned results (cf. Figures 8 and 9) confirm that the electrode design and the filling process can have a huge effect on the battery performance. As was shown previously in experiments [11, 14] and simulations [11, 33], especially the structural properties of the electrodes play an important role. The larger the pores are and the better the connectivity of the pore space is, the better is the effective ionic conductivity and the more surface area remains electrochemically active. These effects can even be enhanced when increasing the wettability of the solid electrode components. Thus, the results indicate, that increasing the power density by calendering the electrodes increases the amount of entrapped gas which leads to a tortuosity increase and finally a reduced battery capacity.

5.4. Permeability

As mentioned before, the permeability is a measure for the fluid mobility and can be used to estimate the effort for displacing entrapped gas agglomerates from electrodes. The permeabilities of the electrolyte and the residual gas phase at the end of the filling process are shown in Figure 10. The corresponding numerical results are also given in Table 3.

From Figure 10 two general observations can be concluded: 1) The permeabilities for cases without binder (IDs 1−8, 15, and 16) are about one order of magnitude larger than for cases with binder (IDs 9−14). 2) In most of the cases the permeability of the gas phase is about one order of magnitude smaller than the electrolyte permeability.

Both effects are mainly influenced by the solid-fluid interfacial contact area and the connectivity of the fluid phase [44]. An increasing solid-fluid contact area increases the flow resistance, thus reducing the fluid mobility [44, 64]. In contrast, a better connectivity enhances the mobility [44, 69]. Electrodes without binder, and thus with less solid material, exhibit a smaller specific solid-fluid contact area, and therefore have larger permeabilities. The residual gas phase, which has a remarkably smaller volume fraction than the electrolyte, has a low connectivity, and thus a lower permeability.

Beside the two aforementioned parameters, also structural properties [70–72], the fluid saturation, the wettability of the solids [44, 64, 70, 73], and the fluid-fluid interfacial area [44, 69, 74] affect the permeability. Apart from the fluid-fluid interfacial area, all other effects are shown in Figure 10 and are discussed in the following.

Large particle sizes (ID 3) and a large volume fraction of the active material (ID 5) result in the largest values of the permeabilities k_y^{E} and k_y^{G}. In both cases the pores are comparable in size which leads to a small solid-fluid contact area and a low flow resistance [72]. Moreover, the amount of residual gas phase is low for both structures (cf. Figure 6). Thus, the connectivity is poor which typically leads to a decreasing permeability. However, here, the effect is dominated by the drag of the engulfing electrolyte phase leading to large values of k_y^{G}. This effect has already been observed experimentally [69]. It is also reproduced by the electrode structures with binder (IDs 9−11) where a larger inner volume fraction causes larger permeabilities.

An increasing wettability results from a strong solid-fluid adhesion force. Thus, the wetting phase is highly attracted by the solid. This leads to an increasing solid-fluid in-

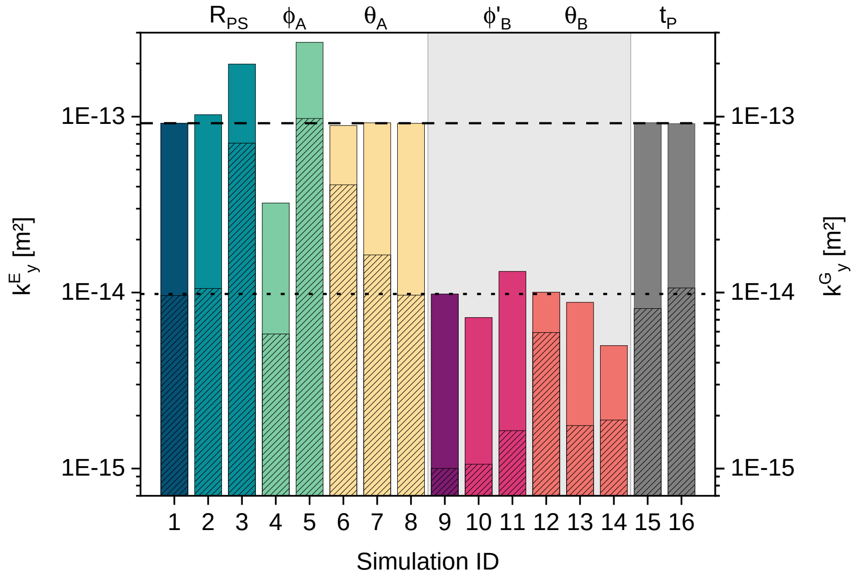

Figure 10: Overview of the electrolyte permeability k_y^{E} and the gas permeability k_y^{G} at the end of the filling process. The values of k_y^{E} are depicted with the colored bars and related to the left ordinate axis. The values of k_y^{G} are depicted with the hatched bars and related to the right ordinate axis. The meaning of the colors is identical to those from Figure 5. The horizontal dashed and dotted line represent k_y^{E} of ID 1 and ID 9, respectively.

terface and a decreasing fluid mobility. The opposite is valid for the non-wetting phase [22, 44]. However, this effect is known to compete with the fluid connectivity which increases the fluid mobility [44]. This is also shown in Figure 10; the electrolyte permeability seems to be hardly affected by the wettability of the active material (IDs 1, 6−8). But when also taking into account the electrolyte saturation $S_{\mathrm{final}}^{\mathrm{E}}$ (cf. Figure 6) the link is not so clear anymore. As the contact angle θ_{A} increases, the saturation decreases and results in a reduced electrolyte connectivity. Thus, only an apparent effect is observed here. In fact, while the increased contact angle enhances the electrolyte mobility, the decreased connectivity compensates that effect. It is even more pronounced for simulations in which the binder wettability was varied (IDs 9, 12−14). There, increasing the contact angle θ_{B} counter-intuitively even reduces the electrolyte permeability. The same two competing effects affect the gas phase, although they are less apparent. Thus, leading to an increased gas permeability for lower contact angles or a better electrolyte wettability.

6. Conclusion

In this study, LBM simulations were used to improve the understanding of electrolyte filling processes on the pore scale. Therefore, a new lattice Boltzmann model for studying multi-phase fluid flow simultaneously in pores of different length scales is presented. This model was applied to study the electrolyte filling of realistic 3D lithium-ion cathodes with and without binder. Similarly other battery components as well as complete cells can be analyzed. Moreover, the methodology is universal and can be generally applied to other energy storage devices such as metal-air batteries, flow batteries or fuel cells. The influence of a wide range of relevant structural and physico-chemical properties as well as process parameters was studied. In particular, 16 large-scale simulations were conducted in which the particle size, volume fraction, and wettability of the active material, the distribution, inner volume fraction, and wettability of the binder, as well as the process time were varied. Pressure-saturation curves were determined for each simulation. They show a systematic entrapment of residual gas, i.e. an incomplete electrolyte saturation. The extent of which depends on the different influencing factors. A detailed analysis was conducted to understand the interdependencies of the amount, the spatial distribution, and size distributions of the gas agglomerates, as well as their effect on transport properties and active surfaces.

In general, the findings of the present work indicate that the filling process is mainly influenced by the structural properties of the electrodes and can additionally be optimized by increasing the surface wettability. The influence of the process time is subordinate for the values studied in the present work. At the end of the filling process, most of the electrodes contained 10 % or less residual gas phase. Regarding the reduction of the gas entrapment, good results were observed for large pores with a narrow pore size distribution and a hydrophilic active material. The amount of residual gas phase was further reduced when adding a strongly wetting binder. Increasing the filling speed resulted in the entrapment of a slightly larger amount of medium-sized gas agglomerates. The worst saturation was observed for the electrode containing a dewetting binder. There, at the end of the filling process 37 % of the pore space were still occupied by gas phase.

A detailed analysis of the position and distribution of the residual gas phase was conducted to understand the impact of an incomplete filling on the battery performance. It was shown that gas agglomerates increase ionic transport pathways in electrodes leading to a decrease of the effective ionic conductivity. Moreover, gas agglomerates reduce the electrochemically active surface area. Both effects increase overpotentials during battery operation and have a negative impact on the specific battery capacity. The most favorable results were observed for electrodes with large pores and a good connectivity of the pore space as well as a good wettability of the solid electrode components. This indicates that calendering the electrodes to increase the energy density could in fact reduce the saturation of the pore space which in turn has an additional negative effect on the power density of the battery.

Finally, it was shown which efforts are necessary to displace gas agglomerates from electrodes. For that, the permeabilities of both electrolyte and gas phase at the end of the filling process were determined. The findings indicate that the binder decreases the mobility of the gas agglomerates. The largest permeabilities were observed for large pores with a narrow pore size distribution and a wetting active material.

Altogether, it is shown that the new lattice Boltzmann model yields a detailed insight and a profound understanding of the influencing factors of filling processes on the pore scale. The results are promising and can especially be used to support electrode and electrolyte design as well as the filling process.

Acknowledgement

The authors gratefully acknowledge financial support from the European Union's Horizon 2020 Research and Innovation Programme within the project "DEFACTO" under the grant number 875247. Furthermore, the presented work was financially supported by the Bundesministerium für Bildung und Forschung (BMBF) within the project HiStructures under the grant number 03XP0243D. The simulations were carried out on the Hawk at the High Performance Computing Center Stuttgart (HLRS) under the grant LaBoRESys, and on JUSTUS 2 at the University Ulm under the grant INST 40/467-1 FUGG.

A. LBM Details

A.1. D3Q19 Velocity Set

The D3Q19 velocity set used in the present work is given by

$$
\begin{aligned}
&[\mathbf{c}_0, \mathbf{c}_1, \mathbf{c}_2, \mathbf{c}_3, \mathbf{c}_4, \mathbf{c}_5, \mathbf{c}_6, \mathbf{c}_7, \mathbf{c}_8, \mathbf{c}_9, \mathbf{c}_{10}, \mathbf{c}_{11}, \mathbf{c}_{12}, \mathbf{c}_{13}, \mathbf{c}_{14}, \mathbf{c}_{15}\mathbf{c}_{16}, \mathbf{c}_{17}, \mathbf{c}_{18}] \qquad \text{(A.1)}\\
&= \frac{\Delta x}{\Delta t}\begin{bmatrix} 0 & -1 & 0 & 0 & 1 & 0 & 0 & -1 & -1 & -1 & -1 & 0 & 0 & 1 & 1 & 1 & 1 & 0 & 0 \\ 0 & 0 & -1 & 0 & 0 & 1 & 0 & -1 & 1 & 0 & 0 & -1 & -1 & 1 & -1 & 0 & 0 & 1 & 1 \\ 0 & 0 & 0 & -1 & 0 & 0 & 1 & 0 & 0 & -1 & 1 & -1 & 1 & 0 & 0 & 1 & -1 & 1 & -1 \end{bmatrix}
\end{aligned}
$$

A.2. Equilibrium Distribution Function

The Maxwell-Boltzmann equilibrium distribution function is determined as

$$f_i^{eq}(\rho, \mathbf{u}) = w_i \rho \left[1 + \frac{\mathbf{c}_i \mathbf{u}}{c_s^2} + \frac{(\mathbf{c}_i \mathbf{u})^2}{2c_s^4} - \frac{\mathbf{u}\mathbf{u}}{2c_s^2}\right]. \qquad \text{(A.2)}$$

Here, w_i are the corresponding lattice specific weights ($w_i = 1/3$ for $i = 0$, $w_i = 1/18$ for $i = 1 \ldots 6$, and $w_i = 1/36$ for $i = 7 \ldots 18$). The lattice speed of sound is $c_s = 1/\sqrt{3}$.

A.3. Physical Quantities

From the distribution function $\boldsymbol{f}$, different relevant macroscopic properties can be determined locally. Those are, e.g., the density

$$\rho = \sum_i f_i, \qquad \text{(A.3)}$$

and the macroscopic flow velocity

$$\mathbf{u} = \frac{1}{\rho} \sum_i f_i \mathbf{c}_i. \qquad \text{(A.4)}$$

The total pressure of the mixture follows the ideal gas law which is extended by the interaction contribution of both components which dominates at the fluid-fluid interface:

$$p(\mathbf{x}) = c_s^2 \left[\rho(\mathbf{x}) + G_{\text{inter}}^{\sigma\bar{\sigma}} \rho^{\sigma}(\mathbf{x}) \rho^{\bar{\sigma}}(\mathbf{x}) \Delta t^2\right]. \qquad \text{(A.5)}$$

A.4. Correlation for the Contact Angle

Following Huang *et al.* [41], the interaction parameters of the wetting (w) and nonwetting (nw) phase are typically related as $G_{\text{ads}}^{\text{nw}} = -G_{\text{ads}}^{\text{w}}$. Under this condition, the contact angle can be determined as [41]

$$\cos\theta = \frac{4G_{\text{ads}}^{\text{nw}}}{G_{\text{inter}}(\rho^{\text{w}} - \rho_{\text{dis}}^{\text{nw}})}. \qquad \text{(A.6)}$$

References

[1] D. L. Wood, J. Li, C. Daniel, Prospects for reducing the processing cost of lithium ion batteries, Journal of Power Sources 275 (2015) 234–242. `doi:10.1016/j.jpowsour.2014.11.019`.

[2] J. B. Habedank, F. J. Günter, N. Billot, R. Gilles, T. Neuwirth, G. Reinhart, M. F. Zaeh, Rapid electrolyte wetting of lithium-ion batteries containing laser structured electrodes: in situ visualization by neutron radiography, The International Journal of Advanced Manufacturing Technology 102 (9) (2019) 2769–2778. `doi:10.1007/s00170-019-03347-4`.

[3] T. Knoche, V. Zinth, M. Schulz, J. Schnell, R. Gilles, G. Reinhart, In situ visualization of the electrolyte solvent filling process by neutron radiography, Journal of Power Sources 331 (2016) 267–276. `doi:10.1016/j.jpowsour.2016.09.037`.

[4] W. Weydanz, H. Reisenweber, A. Gottschalk, M. Schulz, T. Knoche, G. Reinhart, M. Masuch, J. Franke, R. Gilles, Visualization of electrolyte filling process and influence of vacuum during filling for hard case prismatic lithium ion cells by neutron imaging to optimize the production process, Journal of Power Sources 380 (2018) 126–134. `doi:10.1016/j.jpowsour.2018.01.081`.

[5] T. Knoche, F. Surek, G. Reinhart, A process model for the electrolyte filling of lithium-ion batteries, Procedia CIRP 41 (2016) 405–410. `doi:10.1016/j.procir.2015.12.044`.

[6] A. Schilling, S. Wiemers-Meyer, V. Winkler, S. Nowak, B. Hoppe, H. H. Heimes, K. Dröder, M. Winter, Influence of separator material on infiltration rate and wetting behavior of lithium-ion batteries, Energy Technology 8 (2) (2020) 1–7. `doi:10.1002/ente.201900078`.

[7] M. Lanz, E. Lehmann, R. Imhof, I. Exnar, P. Novák, In situ neutron radiography of lithium-ion batteries during charge/discharge cycling, Journal of Power Sources 101 (2) (2001) 177–181. `doi:10.1016/S0378-7753(01)00706-6`.

[8] R. Imhof, P. Novák, In situ investigation of the electrochemical reduction of carbonate electrolyte solutions at graphite electrodes, Journal of The Electrochemical Society 145 (4) (1998) 1081–1087. `doi:10.1149/1.1838420`.

[9] A. Schilling, P. Gümbel, M. Möller, F. Kalkan, F. Dietrich, K. Dröder, X-ray based visualization of the electrolyte filling process of lithium ion batteries, Journal of The Electrochemical Society 166 (3) (2019) A5163–A5167. `doi:10.1149/2.0251903jes`.

[10] S. Müller, J. Eller, M. Ebner, C. Burns, J. Dahn, V. Wood, Quantifying inhomogeneity of lithium ion battery electrodes and its influence on electrochemical performance, Journal of The Electrochemical Society 165 (2) (2018) A339–A344. `doi:10.1149/2.0311802jes`.

[11] C. Sauter, R. Zahn, V. Wood, Understanding electrolyte infilling of lithium ion batteries, Journal of The Electrochemical Society 167 (10) (2020) 100546. `doi:10.1149/1945-7111/ab9bfd`.

[12] M. S. Wu, T. L. Liao, Y. Y. Wang, C. C. Wan, Assessment of the wettability of porous electrodes for lithium-ion batteries, Journal of Applied Electrochemistry 34 (8) (2004) 797–805. `doi:10.1023/B:JACH.0000035599.56679.15`.

[13] S. S. Zhang, A review on electrolyte additives for lithium-ion batteries, Journal of Power Sources 162 (2 SPEC. ISS.) (2006) 1379–1394. `doi:10.1016/j.jpowsour.2006.07.074`.

[14] A. Davoodabadi, C. Jin, D. L. Wood III, T. J. Singler, J. Li, On electrolyte wetting through lithium-ion battery separators, Extreme Mechanics Letters 40 (2020) 100960. `doi:10.1016/j.eml.2020.100960`.

[15] F. J. Günter, J. B. Habedank, D. Schreiner, T. Neuwirth, R. Gilles, G. Reinhart, Introduction to electrochemical impedance spectroscopy as a measurement method for the wetting degree of lithium-ion cells, Journal of The Electrochemical Society 165 (14) (2018) A3249–A3256. `doi:10.1149/2.0081814jes`.

[16] S. Chen, G. D. Doolen, Lattice Boltzmann method for fluid flows, Annual Review of Fluid Mechanics 30 (1) (1998) 329–364. `doi:10.1146/annurev.fluid.30.1.329`.

[17] T. Krueger, H. Kusumaatmaja, A. Kuzmin, O. Shardt, G. Silva, E. Viggen, The Lattice Boltzmann Method: Principles and Practice, Springer, 2016.

[18] L. Chen, Q. Kang, Y. Mu, Y. L. He, W. Q. Tao, A critical review of the pseudopotential multiphase lattice Boltzmann model: Methods and applications, International Journal of Heat and Mass Transfer 76 (2014) 210–236. `doi:10.1016/j.ijheatmasstransfer.2014.04.032`.

[19] H. Liu, Q. Kang, C. R. Leonardi, S. Schmieschek, A. Narváez, B. D. Jones, J. R. Williams, A. J. Valocchi, J. Harting, Multiphase lattice Boltzmann simulations for porous media applications: A review, Computational Geosciences 20 (4) (2016) 777–805. `doi:10.1007/s10596-015-9542-3`.

[20] X. Shan, H. Chen, Lattice Boltzmann model for simulating flows with multiple phases and components, Physical Review E 47 (3) (1993) 1815–1819. `doi:10.1103/PhysRevE.47.1815`.

[21] F. Diewald, M. P. Lautenschlaeger, S. Stephan, K. Langenbach, C. Kuhn, S. Seckler, H.-J. Bungartz, H. Hasse, R. Müller, Molecular dynamics and phase field simulations of droplets on surfaces with wettability gradient, Computer Methods in Applied Mechanics and Engineering 361 (2020) 112773. `doi:10.1016/j.cma.2019.112773`.

[22] M. P. Lautenschlaeger, H. Hasse, Thermal, caloric and transport properties of the Lennard–Jones truncated and shifted fluid in the adsorbed layers at dispersive solid walls, Molecular Physics 118 (9-10) (2020) e1669838. `doi:10.1080/00268976.2019.1669838`.

[23] S. Becker, H. M. Urbassek, M. Horsch, H. Hasse, Contact angle of sessile drops in Lennard-Jones systems, Langmuir 30 (45) (2014) 13606–13614. `doi:10.1021/la503974z`.

[24] M. P. Lautenschlaeger, H. Hasse, Transport properties of the Lennard-Jones truncated and shifted fluid from non-equilibrium molecular dynamics simulations, Fluid Phase Equilibria 482 (2019) 38–47. `doi:10.1016/j.fluid.2018.10.019`.

[25] M. P. Lautenschlaeger, H. Hasse, Shear-rate dependence of thermodynamic properties of the Lennard-Jones truncated and shifted fluid by molecular dynamics simulations, Physics of Fluids 31 (6) (2019). `doi:10.1063/1.5090489`.

[26] Z. Jiang, Z. Qu, Lattice Boltzmann simulation of ion and electron transport in lithium ion battery porous electrode during discharge process, Energy Procedia 88 (2016) 642–646. `doi:10.1016/j.egypro.2016.06.091`.

[27] T. Danner, S. Eswara, V. P. Schulz, A. Latz, Characterization of gas diffusion electrodes for metal-air batteries, Journal of Power Sources 324 (2016) 646–656. `doi:10.1016/j.jpowsour.2016.05.108`.

[28] Z. Y. Jiang, Z. G. Qu, L. Zhou, W. Q. Tao, A microscopic investigation of ion and electron transport in lithium-ion battery porous electrodes using the lattice Boltzmann method, Applied Energy 194 (2017) 530–539. `doi:10.1016/j.apenergy.2016.10.125`.

[29] Z. Y. Jiang, Z. G. Qu, L. Zhou, Lattice Boltzmann simulation of ion and electron transport during the discharge process in a randomly reconstructed porous electrode of a lithium-ion battery, International Journal of Heat and Mass Transfer 123 (2018) 500–513. `doi:10.1016/j.ijheatmasstransfer.2018.03.004`.

[30] S. G. Lee, D. H. Jeon, B. M. Kim, J. H. Kang, C.-J. Kim, Lattice Boltzmann simulation for electrolyte transport in porous electrode of lithium ion batteries, Journal of The Electrochemical Society 160 (4) (2013) H258–H265. `doi:10.1149/2.017306jes`.

[31] S. G. Lee, D. H. Jeon, Effect of electrode compression on the wettability of lithium-ion batteries, Journal of Power Sources 265 (2014) 363–369. `doi:10.1016/j.jpowsour.2014.04.127`.

[32] D. H. Jeon, Wettability in electrodes and its impact on the performance of lithium-ion batteries, Energy Storage Materials 18 (2019) 139–147. `doi:10.1016/j.ensm.2019.01.002`.

[33] A. Shodiev, E. Primo, O. Arcelus, M. Chouchane, M. Osenberg, A. Hilger, I. Manke, J. Li, A. A. Franco, Insight on electrolyte infiltration of lithium ion battery electrodes

by means of a new three-dimensional-resolved lattice Boltzmann model, Energy Storage Materials 38 (2021) 80–92. `doi:10.1016/j.ensm.2021.02.029`.

[34] S. K. Mohammadian, Y. Zhang, Improving wettability and preventing Li-ion batteries from thermal runaway using microchannels, International Journal of Heat and Mass Transfer 118 (2018) 911–918. `doi:10.1016/j.ijheatmasstransfer.2017.11.063`.

[35] G. G. Pereira, Grayscale lattice Boltzmann model for multiphase heterogeneous flow through porous media, Physical Review E 93 (6) (2016) 1–14. `doi:10.1103/PhysRevE.93.063301`.

[36] G. G. Pereira, A multiphase single relaxation time lattice Boltzmann model for heterogeneous porous media, Applied Mathematical Modelling 44 (2017) 160–174. `doi:10.1016/j.apm.2016.11.009`.

[37] G. G. Pereira, Fluid flow, relative permeabilities and capillary pressure curves through heterogeneous porous media, Applied Mathematical Modelling 75 (2019) 481–493. `doi:10.1016/j.apm.2019.05.050`.

[38] S. D. Walsh, H. Burwinkle, M. O. Saar, A new partial-bounceback lattice Boltzmann method for fluid flow through heterogeneous media, Computers & Geosciences 35 (6) (2009) 1186–1193. `doi:10.1016/j.cageo.2008.05.004`.

[39] M. G. Schaap, M. L. Porter, B. S. Christensen, D. Wildenschild, Comparison of pressure-saturation characteristics derived from computed tomography and lattice Boltzmann simulations, Water Resources Research 43 (12) (2007) 1–15. `doi:10.1029/2006WR005730`.

[40] Y.-L. He, Q. Liu, Q. Li, W.-Q. Tao, Lattice Boltzmann methods for single-phase and solid-liquid phase-change heat transfer in porous media: A review, International Journal of Heat and Mass Transfer 129 (2019) 160–197. `doi:10.1016/j.ijheatmasstransfer.2018.08.135`.

[41] H. Huang, D. T. Thorne, M. G. Schaap, M. C. Sukop, Proposed approximation for contact angles in Shan-and-Chen-type multicomponent multiphase lattice Boltzmann models, Physical Review E 76 (6) (2007) 1–6. `doi:10.1103/PhysRevE.76.066701`.

[42] N. S. Martys, H. Chen, Simulation of multicomponent fluids in complex three-dimensional geometries by the lattice Boltzmann method, Physical Review E 53 (1) (1996) 743–750. `doi:10.1103/PhysRevE.53.743`.

[43] Z. Li, S. Galindo-Torres, G. Yan, A. Scheuermann, L. Li, A lattice Boltzmann investigation of steady-state fluid distribution, capillary pressure and relative permeability of a porous medium: Effects of fluid and geometrical properties, Advances in Water Resources 116 (2018) 153–166. `doi:10.1016/j.advwatres.2018.04.009`.

[44] C. J. Landry, Z. T. Karpyn, O. Ayala, Relative permeability of homogenous-wet and mixed-wet porous media as determined by pore-scale lattice Boltzmann modeling, Water Resources Research 50 (5) (2014) 3672–3689. `doi:10.1002/2013WR015148`.

[45] J. Latt, O. Malaspinas, D. Kontaxakis, A. Parmigiani, D. Lagrava, F. Brogi, M. B. Belgacem, Y. Thorimbert, S. Leclaire, S. Li, F. Marson, J. Lemus, C. Kotsalos, R. Conradin, C. Coreixas, R. Petkantchin, F. Raynaud, J. Beny, B. Chopard, Palabos: parallel Lattice Boltzmann solver, Computers & Mathematics with Applications 81 (2021) 334–350. `doi:10.1016/j.camwa.2020.03.022`.

[46] D. Westhoff, I. Manke, V. Schmidt, Generation of virtual lithium-ion battery electrode microstructures based on spatial stochastic modeling, Computational Materials Science 151 (2018) 53–64. `doi:10.1016/j.commatsci.2018.04.060`.

[47] S. Hein, T. Danner, D. Westhoff, B. Prifling, R. Scurtu, L. Kremer, A. Hoffmann, A. Hilger, M. Osenberg, I. Manke, M. Wohlfahrt-Mehrens, V. Schmidt, A. Latz, Influence of conductive additives and binder on the impedance of lithium-ion battery electrodes: Effect of morphology, Journal of The Electrochemical Society 167 (1) (2020) 013546. `doi:10.1149/1945-7111/ab6b1d`.

[48] J. Mościński, M. Bargieł, Z. Rycerz, P. Jakobs, The force-biased algorithm for the irregular close packing of equal hard spheres, Molecular Simulation 3 (1989) 201–212. `doi:10.1080/08927028908031373`.

[49] A. Bezrukov, M. Bargieł, D. Stoyan, Statistical analysis of simulated random packings

of spheres, Particle & Particle Systems Characterization 19 (2) (2002) 111–118. `doi:10.5566/ias.v20.p203-206`.

[50] J. Feinauer, A. Spettl, I. Manke, S. Strege, A. Kwade, A. Pott, V. Schmidt, Structural characterization of particle systems using spherical harmonics, Materials Characterization 106 (2015) 123–133. `doi:10.1016/j.matchar.2015.05.023`.

[51] J. Feinauer, T. Brereton, A. Spettl, M. Weber, I. Manke, V. Schmidt, Stochastic 3D modeling of the microstructure of lithium-ion battery anodes via Gaussian random fields on the sphere, Computational Materials Science 109 (2015) 137–146. `doi:10.1016/j.commatsci.2015.06.025`.

[52] P. Soille, Morphological Image Analysis: Principles and Applications, 2nd Edition, Springer, New York, 2003. `doi:10.1007/978-3-662-05088-0`.

[53] O. Falode, E. Manuel, Wettability effects on capillary pressure, relative permeability, and irredcucible saturation using porous plate, Journal of Petroleum Engineering 2014 (2014) 1–12. `doi:10.1155/2014/465418`.

[54] T. Akai, A. M. Alhammadi, M. J. Blunt, B. Bijeljic, Modeling oil recovery in mixed-wet rocks: Pore-scale comparison between experiment and simulation, Transport in Porous Media 127 (2) (2019) 393–414. `doi:10.1007/s11242-018-1198-8`.

[55] C. Pan, M. Hilpert, C. T. Miller, Lattice Boltzmann simulation of two-phase flow in porous media, Water Resources Research 40 (1) (2004) 1–14. `doi:10.1029/2003WR002120`.

[56] O. Stenzel, O. M. Pecho, L. Holzer, M. Neumann, V. Schmidt, Predicting effective conductivities based on geometric microstructure characteristics, AIChE Journal 62 (5) (2016) 1834–1843. `doi:10.1002/aic.15160`.

[57] M. Neumann., O. Stenzel, F. Willot, L. Holzer, V. Schmidt, Quantifying the influence of microstructure on effective conductivity and permeability: virtual materials testing, International Journal of Solids and Structures 184 (2020) 211–220. `doi:10.1016/j.ijsolstr.2019.03.028`.

[58] D. Jungnickel, Graphs, Networks and Algorithms, 3rd Edition, Springer, Berlin, 2013. `doi:10.1007/978-3-642-32278-5`.

[59] M. Neumann, C. Hirsch, J. Staněk, V. Beneš, V. Schmidt, Estimation of geodesic tortuosity and constrictivity in stationary random closed sets, Scandinavian Journal of Statistics 46 (3) (2019) 848–884. `doi:10.1111/sjos.12375`.

[60] D. A. G. Bruggeman, Berechnung verschiedener physikalischer Konstanten von heterogenen Substanzen. I. Dielektrizitätskonstanten und Leitfähigkeiten der Mischkörper aus isotropen Substanzen, Annalen der Physik 416 (7) (1935) 636–664. `doi:10.1002/andp.19354160705`.

[61] A. Vadakkepatt, B. Trembacki, S. R. Mathur, J. Y. Murthy, Bruggeman's exponents for effective thermal conductivity of lithium-ion battery electrodes, Journal of The Electrochemical Society 163 (2) (2015) A119–A130. `doi:10.1149/2.0151602jes`.

[62] K. K. Patel, J. M. Paulsen, J. Desilvestro, Numerical simulation of porous networks in relation to battery electrodes and separators, Journal of Power Sources 122 (2) (2003) 144–152. `doi:10.1016/S0378-7753(03)00399-9`.

[63] K. Schladitz, J. Ohser, W. Nagel, Measuring intrinsic volumes in digital 3D images, in: A. Kuba, L. Nyúl, K. Palágyi (Eds.), 13th International Conference Discrete Geometry for Computer Imagery, Springer, 2007, pp. 247–258. `doi:10.1007/11907350_21`.

[64] H. Li, C. Pan, C. T. Miller, Pore-scale investigation of viscous coupling effects for two-phase flow in porous media, Physical Review E 72 (2) (2005) 1–14. `doi:10.1103/PhysRevE.72.026705`.

[65] J. Avendaño, N. Lima, A. Quevedo, M. Carvalho, Effect of surface wettability on immiscible displacement in a microfluidic porous media, Energies 12 (4) (2019) 664. `doi:10.3390/en12040664`.

[66] H. Huang, J. J. Huang, X. Y. Lu, Study of immiscible displacements in porous media using a color-gradient-based multiphase lattice Boltzmann method, Computers and Fluids 93 (2014) 164–172. `doi:10.1016/j.compfluid.2014.01.025`.

[67] R. Lenormand, E. Touboul, C. Zarcone, Numerical models and experiments on immiscible displacements in porous media, Journal of Fluid Mechanics 189 (1988) 165–187. `doi:10.1017/S0022112088000953`.

[68] F. G. Wolf, D. N. Siebert, R. Surmas, Influence of the wettability on the residual fluid saturation for homogeneous and heterogeneous porous systems, Physics of Fluids 32 (5) (2020) 052008. `doi:10.1063/5.0004681`.

[69] D. G. Avraam, A. C. Payatakes, Generalized relative permeability coefficients during steady-state two-phase flow in porous media, and correlation with the flow mechanisms, Transport in Porous Media 20 (1) (1995) 135–168. `doi:10.1007/BF00616928`.

[70] Z. Dou, Z. F. Zhou, Numerical study of non-uniqueness of the factors influencing relative permeability in heterogeneous porous media by lattice Boltzmann method, International Journal of Heat and Fluid Flow 42 (2013) 23–32. `doi:10.1016/j.ijheatfluidflow.2013.01.020`.

[71] D. Zhang, K. Papadikis, S. Gu, A lattice Boltzmann study on the impact of the geometrical properties of porous media on the steady state relative permeabilities on two-phase immiscible flows, Advances in Water Resources 95 (2016) 61–79. `doi:10.1016/j.advwatres.2015.12.015`.

[72] M. Ahkami, A. Parmigiani, P. R. Di Palma, M. O. Saar, X. Z. Kong, A lattice Boltzmann study of permeability-porosity relationships and mineral precipitation patterns in fractured porous media, Computational Geosciences 24 (5) (2020) 1865–1882. `doi:10.1007/s10596-019-09926-4`.

[73] A. Ghassemi, A. Pak, Numerical study of factors influencing relative permeabilities of two immiscible fluids flowing through porous media using lattice Boltzmann method, Journal of Petroleum Science and Engineering 77 (1) (2011) 135–145. `doi:10.1016/j.petrol.2011.02.007`.

[74] Z. Li, S. Galindo-Torres, G. Yan, A. Scheuermann, L. Li, Pore-scale simulations of simultaneous steady-state two-phase flow dynamics using a lattice Boltzmann model:

Interfacial area, capillary pressure and relative permeability, Transport in Porous Media 129 (1) (2019) 295–320. `doi:10.1007/s11242-019-01288-w`.